

Review

Terahertz Field Confinement in Nonlinear Metamaterials and Near-Field Imaging

George R. Keiser ^{1,*}  and Pernille Klarskov ^{2,*}

¹ Department of Physics, Washington College, Chestertown, MD 21620, USA

² Department of Engineering, Aarhus University, 8200 Aarhus N., Denmark

* Correspondence: gkeiser2@washcoll.edu (G.R.K.); klarskov@eng.au.dk (P.K.)

Received: 15 December 2018; Accepted: 18 February 2019; Published: 28 February 2019



Abstract: This article reviews recent advances in terahertz science and technology that rely on confining the energy of incident terahertz radiation to small, very sub-wavelength sized regions. We focus on two broad areas of application for such field confinement: metamaterial-based nonlinear terahertz devices and terahertz near-field microscopy and spectroscopy techniques. In particular, we focus on field confinement in: terahertz nonlinear absorbers, metamaterial enhanced nonlinear terahertz spectroscopy, and in sub-wavelength terahertz imaging systems.

Keywords: terahertz; field confinement; nonlinear; metamaterials; near-field imaging

1. Introduction

The terahertz (THz) frequency portion of the electromagnetic spectrum consists of light frequencies between 100 GHz and 10 THz, and uniquely bridges the worlds of ultrahigh frequency (UHF) electronics and photonics. This intermediate nature of THz light is inherently promising for applications to broadband communications engineering and spectroscopy. However, realizing this promise requires overcoming challenges in the generation, detection and manipulation of THz light [1]. Connecting the realms of UHF and photonics means that THz technology lives entirely in neither. THz photonics necessarily involves new hybrid technologies and is an endeavor as much in electronics engineering as it is in photonics engineering.

The past several decades brought much success in building this new field of THz photonics and THz research is now arguably entering a new era [2]. Terahertz wireless communication is quickly becoming viable [3]. Not only are methods for generating continuous wave and THz pulses now standard laboratory techniques but THz pulses with energies in the microjoule range and peak fields between 0.5 and 1 MV/cm are achievable in the lab [4–8]. THz nonlinear optics and nonlinear spectroscopy are now active and growing subdisciplines and the search is on for novel nonlinear materials and devices. One promising avenue for such devices is the field of metamaterials (MMs) engineering, originally used for microwave device engineering, but now applied across the electromagnetic spectrum.

MMs are composites made of sub-wavelength electromagnetic inclusions and respond to light at the design wavelength as a homogenous whole. In the design of nonlinear optics, the near-field properties of the MM inclusions are as important as the far-field response. Most nonlinear THz devices based on MMs or other plasmonic structures implement the nonlinear response by using subwavelength resonator inclusions to confine incident fields, coupling to and amplifying an underlying nonlinearity in either a substrate or material inclusion. Such enhanced THz nonlinearities have applications not just in nonlinear optics [9], but in enhanced sensing and nonlinear pump-probe spectroscopy as well [10].

Concurrently, the ability to enhance THz fields with free-standing metallic probes such as the tips used for scanning tunneling microscopy (STM) or atomic force microscopy (AFM) has also been widely exploited. In a similar way as for MMs, the THz field confinement at the apex of the tip can facilitate extreme nonlinear effects. Intense THz pulses directed onto a sharp metal tip have shown the ability to induce field emission of electrons [11] or even tunnel electrons across an STM junction [12], adding time-resolution to STM techniques where spatial resolutions of down to the sub-nm scale can be achieved in ultra-high vacuum conditions [13,14]. Staying below this extreme tunneling regime with less intense THz pulses, the field confinement of THz light at the apex of a tip has also been used to image samples with a spatial resolution much better than the diffraction-limit of a THz beam. Since diffraction limits the conventional THz imaging resolution to several hundreds of microns, the ability to image with a nanoscale tip apex has revolutionized the field of THz imaging. Today, the diffraction-limit has been beaten by more than four orders of magnitude.

In this paper, we review recent advances in the methods of THz field confinement (FC), focusing on these two broad areas of application: nonlinear THz devices based on MMs and THz near-field imaging techniques. Section 2 focuses on methods of FC involving MMs and their applications. In particular, we focus on FC in nonlinear MM absorbers and MM enhanced nonlinear THz spectroscopy. In Section 3, we then turn to FC when using metallic probes for high-resolution imaging at THz frequencies.

2. Field Confinement and Applications in Terahertz and Infrared Metamaterial Devices

2.1. Background

Interest in THz MMs originally focused almost entirely on far-field optical properties. These far-field properties, in particular the electromagnetic impedance and index of refraction of the MM, can be tailored by controlling the geometry and periodicity of the component inclusions [15]. Research at GHz frequencies initially focused on novel optical properties not found in nature, including the now famous results on perfect lensing [16], negative refractive index [17], electromagnetic cloaking [18], and memory metamaterials [19]. The MM idea spread quickly to higher frequencies, and THz frequencies were especially well suited to metamaterials research. Subwavelength inclusions for THz MMs could be fabricated using standard photolithographic techniques, and novel methods to develop THz optics and devices were needed to fill the THz gap [1]. Excitement grew as MM based absorbers and detectors [20–22], filters [23], wave plates [24], and modulators [25,26] appeared in the literature.

The ability of resonant MM structures to confine incident fields is critical to their application in nonlinear devices and below we provide a short review of the properties of MM FC and how it can be controlled and engineered. We then provide an overview of some keynote applications of MM FC within the fields of THz nonlinear optics and spectroscopy.

FC in THz metamaterials and plasmonics arises from inducing very highly localized charge or current distributions within the MM unit cell. Resonant inclusions such as the common split ring resonator (SRR) and its variants [27] support tightly confined charge distributions and high current densities are thus commonly used in nonlinear MM devices. A simple SRR can be made by cutting a small gap in a ring of conducting material. As a first approximation, the circular SRR can be thought of as a half-wave dipole bent into a ring shape. Incident radiation with a wavelength on the order of

$$\lambda = 2L \quad (1)$$

where L is the circumference of the SRR that will excite a resonant current response in the ring. The resonant current density, in this fundamental mode, will follow a cosine distribution around the circumference of the ring given by:

$$j = j_0 \cos\left(\frac{\pi s}{L}\right) e^{-i\omega t} \quad (2)$$

where s is the arc length around the ring, measured from one end of the split gap to the other. Continuity of charge and current will thus require that an oscillating charge distribution build up on the ends of

the split gap during the resonant excitation. This charge distribution, Q , oscillates 90° out of phase with the current and is largest near the edges of the split gap:

$$Q = Q_0 \sin\left(\frac{\pi S}{L}\right) e^{-i\omega t} \quad (3)$$

Thus, incident radiation at the resonance wavelength will induce a large charge distribution, positive on one end of the gap and negative on the other. The split gap thus acts as a small parallel plate capacitor, inducing a large confined electric field in the gap region that is proportional to the peak charge distribution, Q_0 , and inversely proportional to the length of the gap.

Alternatively, the SRR can be thought of as an LC resonant circuit. The split gap in the ring provides the primary contribution to the capacitance, C , and the ring's self inductance determines L . The resonance frequency is thus approximately

$$f = \frac{1}{2\pi} \sqrt{\frac{1}{LC}} \quad (4)$$

corresponding to the same resonance wavelength as above in Equation (1). These simple models provide a good first approximation to the behavior of the circular SRR's lowest order resonance, and insight into the physical origin of the confined electric fields in the structure. While applied here to a circular ring, this logic is approximately correct for SRR of more complicated geometries as well. If needed, more detailed eigenmode analyses can be used to model the behavior of higher order resonances [28], but for most field confinement applications, the lowest order resonance will suffice.

Figure 1a shows the spatial distribution of confine electric fields in a SRR inclusion. The gap capacitance and self-inductance of the structure determine the lowest order resonance, and are tailored to fall in this simulation near 1 THz. The simulation uses an incident THz pulse traveling into the plane of the page with an electric field polarized perpendicular to the split gap. This geometry excites the fundamental resonance of the structure and induces a large transient current around the SRR and a transient charge distribution on the edges of the split gap.

Figure 1a shows the transient electric field in one unit cell of the SRR metamaterial at the peak of the excitation, while Figure 1b shows the corresponding transient magnetic field peak. Notice the large electric field strength in the gap region of the SRR. The charge distribution on the edges of the split gap acts to confine the incident pulse fields, producing a transient "hot spot" of electric field. A similar effect occurs for the magnetic field, but in a separate region of the structure, near the regions of peak transient current, shown in Figure 1b. The confined electric fields can be up to $10\times$ higher in magnitude than the incident field. In the frequency domain, on resonance components of the incident field can be amplified up to $100\times$ in these regions. Although challenging, it is possible to quantitatively measure the local FC in a subwavelength resonator, for instance, via non-invasive electro-optic imaging techniques [30]. However, this step is not required for the design of MM devices requiring FC. Numerical simulations performed with standard commercial electromagnetics solvers can be used to adequately design and estimate the location and magnitude of the FC in most device designs.

With small enough gap regions, and an incident THz field of ~ 300 kV/cm, confined THz fields high enough to induce permanent mass transfer of the gold in the SRR (see Figure 1c,d) [30], and field electron emission [31] are possible. To date, there have been fewer applications of magnetic field confinement in THz metamaterials, as the electric field confinement is a much larger effect in the SRR due to the narrowness of the gap region. However, this is not a fundamental limitation. Modified resonator structures can be used to achieve optimized magnetic field confinement, including electrical complementary resonators [32].

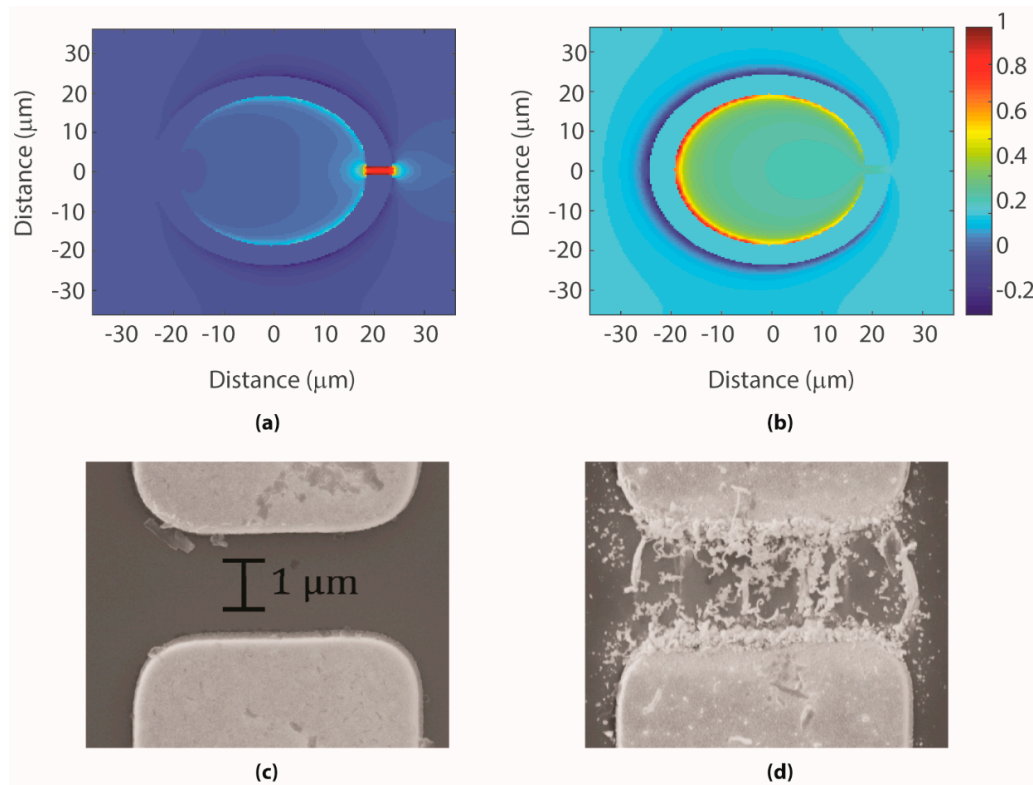


Figure 1. Numerical simulations of the normalized peak (a) electric field and (b) magnetic field distributions in a split ring resonator excited by an incident THz signal. Electric fields are confined to the capacitive gap region, while magnetic fields are confined near the areas of high current density in the resonator. (c,d) Before and after pictures showing mass transfer of gold patterning in a metamaterial antenna structure. Mass transfer is induced by the highly confined resonant fields in the 1 μm thick gap region. Reproduced from [29].

2.2. Active Control and Turning of Field Confinement in Metamaterials

Active control and tuning of FC in metamaterials is also possible. Many of the methods used to the frequency response or bandwidth of MM devices, including active electrical tuning [33] and structural tuning via MEMs actuation [34,35], can also be used to modify the local electric fields in the unit cell. As an example, Figure 2 shows a proof of principle study on tuning the FC in the gap region of a SRR [36]. The SRR array is fabricated above an array of non-resonant gold conducting rings, which act to dampen the resonant response of the SRR. Laterally shifting the SRR away from its closed ring neighbor alters the oscillator strength of the resonance and notably changes the strength of the in-gap resonant electric field. Figure 2b shows that, as the lateral displacement of the SRRs increases, the on-resonance fields inside the SRR gap drops from near $100\times$ the incident field strength to $60\times$. The ability to precisely control and tune field strength via the MM geometry is essential for applications to nonlinear THz devices and enhanced sensing and spectroscopic techniques. In the next section, we highlight several keynote results in the realm of THz MM nonlinear devices.

While the realization of nonlinear MMs at THz frequencies is a more recent phenomenon, the theoretical groundwork was laid much earlier and applications at microwave frequencies have been common for some time [37–43]. Implementations of nonlinear MMs require that the design of the unit cell include some kind of a subwavelength nonlinear element. At microwave frequencies or lower, this can be accomplished, for instance, by including diode/varactors [44–46], or deformable substrates [47] into the design of a SRR or other subwavelength inclusion. For many applications, this approach works well, and has allowed for engineering of a range of nonlinear phenomena including wave mixing [43], and second harmonic generation [48], an example of which is shown in Figure 3a.

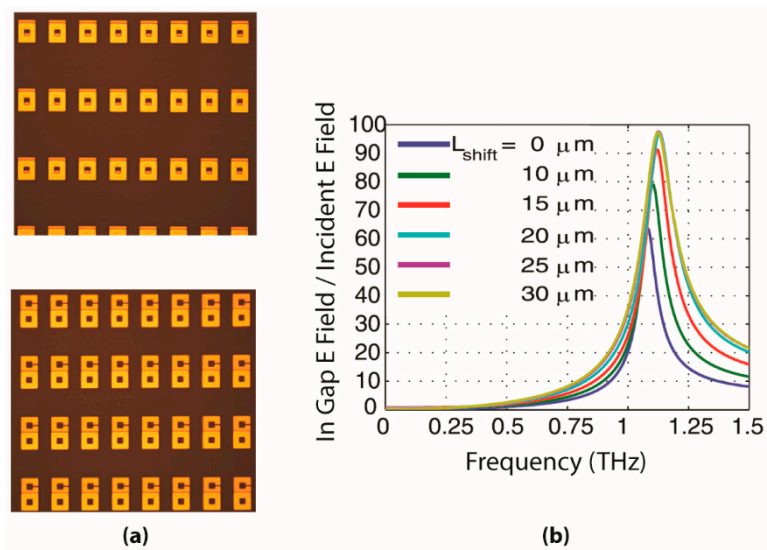


Figure 2. Example of structural tuning of field confinement in a split ring resonator. (a) Photograph of a metamaterial consisting of a SRR array below a closed conducting ring array. (b) Inducing an in-plane shift between the two layers, results in a 40% increase to the magnitude of the electric fields confined in the SRR gap. Reproduced from [36].

2.3. Field Confinement Applications in Nonlinear Metamaterial Devices

For THz frequency applications, the size of subwavelength structures is approximately 10–100 μm , which makes use of nonlinear lumped circuit elements untenable for most applications. Instead, the primary method of implementing nonlinear THz MMs has been to use electric FC to couple incident THz radiation to a resonant nonlinearity in an underlying substrate or material inclusion. The FC acts to enhance the underlying nonlinear response, resulting in nonlinear behavior for incident field strengths much lower than needed to excite the same nonlinear effects without the presence of the MM. THz FC has given rise to materials exhibiting quintessential nonlinear phenomena, including THz second harmonic generation [9] and THz induced optical photoluminescence. An example of the latter, from the Huber group, is shown in Figure 3b [49].

With high field sources, it is possible to see nonlinearities due to FC in many common MM designs, and these nonlinearities can have large effects on the functionality of the device. For instance, the inset in Figure 3c shows an example of a nonlinear MM fabricated on an n-doped GaAs substrate, a substrate commonly used in actively switchable MM devices [50]. Incident excitations on the order of 50 kV/cm excite resonant nonlinearities in the GaAs substrate [51] that arise from inter-valley scattering of carriers [52,53]. Even higher incident fields, coupled with FC in the MM unit cell also induce impact ionization of charge carriers [51,54]. Thus, common active MM devices based on GaAs show a notably altered switchable response at higher incident field strengths. Figure 3c, shows that the modulation range of a switchable MM can drop to near 0 dB for incident THz excitations of >50 kV/cm, due to carrier scattering. The overall depth and strength of the resonant response changes at even higher field strengths, due to impact ionization induced by FC in the MM resonators. Such phenomena highlight the care that must be taken when designing MM devices for high field applications. Of course, the FC approach to nonlinear MMs can extend beyond the THz frequencies and into near infrared and optical applications as well. As shown in Figure 3d, Keren-Sur et al. recently demonstrated a device for nonlinear beam shaping of near IR light based on field confinement in nanoscale SRRs [55].

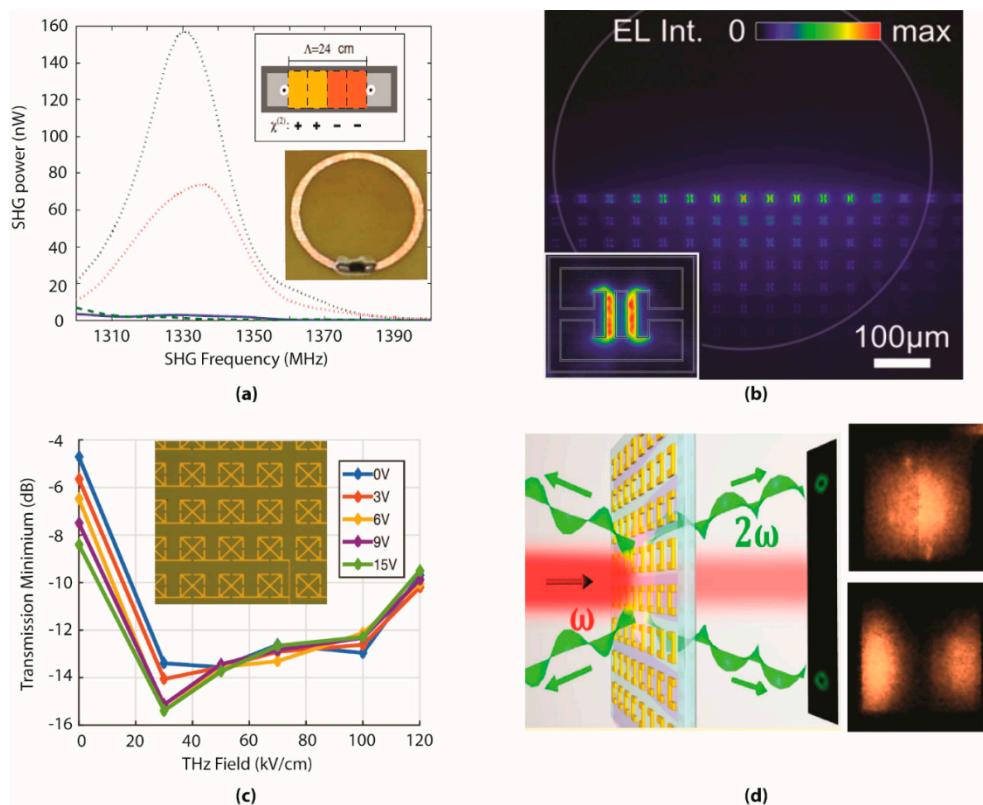


Figure 3. Field confinement in nonlinear metamaterials. (a) A nonlinear metamaterial for second harmonic generation at microwave frequencies. A varactor in the SRR capacitive gap (lower right inset) gives rise to the nonlinear response. (b) THz induced optical photoluminescence due to field confinement in SRRs (low left inset). Reprinted with permission from [48,49]. Copyright 2011 and 2014, respectively, by the American Physical Society. (c) Actively tunable MM devices on GaAs (center inset) substrates show strong nonlinear responses due to high incident fields and field confinement. For high incident fields, the overall modulation range drops to 0 dB, due to nonlinear effects [50]. (d) Nonlinear MMs in the near IR can also be implemented using field confinement. Here, field confinement induces second harmonic generation of an 800 nm beam and beam shaping of the 400 nm output. Reprinted with permission from [55]. Copyright 2016 by the American Chemical Society.

One promising application of field confinement in MM devices is in the field of absorbers and sensors. For many years, high Q factor resonances and confined fields of MMs have been used to enhance the response of detectors at THz and IR wavelengths and as a means of detecting amounts of trace chemicals [56–60]. Figure 4a,b shows a recent example of such a MM thermal detector for IR applications [61]. This example from Suen et al. [61] uses a MM to confine incident fields onto a piezoelectric layer. The piezoelectric material then responds more strongly to the confined fields compared to the incident signal, significantly reducing noise from temperature fluctuations. Additionally, the resonant nature of the MM also enhances the spectral selectivity of the detector (Figure 4b) without the need for any external filters or dispersive optics.

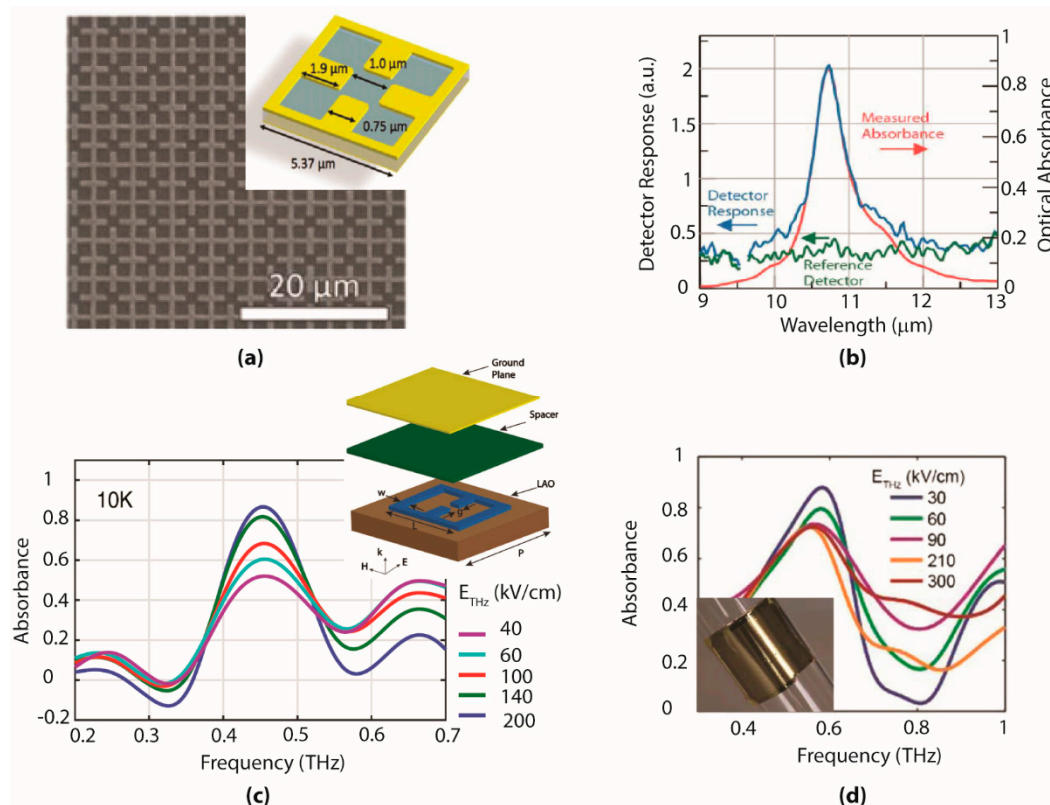


Figure 4. Applications of high fields and field confinement in MM detectors and saturable absorbers. (a) A metamaterial/pyroelectric based IR detector with enhanced sensitivity due to field confinement in the resonator gaps, where a pyroelectric material responds to the local field [61]. (b) Plot of the absorption and response curve for the MM from (a). (c) A THz saturable absorber designed using superconducting MMs (see inset for schematic). The resonant fields in the MM couple the nonlinear response of the YBCO superconducting SRR to produce an absorption peak that depends on the incident THz power, as shown here. Reproduced from [62]. (d) Another example of a THz saturable absorber. Here, small GaAs patches are placed in the confined fields of a metamaterial resonator gap to produce a power dependent absorption peak. The device is fabricated on a flexible polyimide film (see inset) [63].

In particular, THz FC allows for the development of novel MM composites that function as THz saturable absorbers, which have important applications in mode-locked lasers and the generation of ultrafast light sources [64,65]. A MM nonlinear absorber is a type of MM perfect absorber [64], designed to have a power dependent absorption peak through the use of FC and nonlinear material inclusions. A MM perfect absorber is a device that minimizes both reflectance, r , and transmittance, t , at a particular frequency in order to produce a strong absorption band, $A(\omega)$:

$$A(\omega) = 1 - |r(\omega)|^2 - |t(\omega)|^2 \tag{5}$$

The inset in Figure 4c shows a common unit cell design for a THz perfect absorber that operates in reflection [21].

The reflectance from the structure depends strongly on the resonance of the SRR array. The E field of incident THz radiation couples to the SRR fundamental mode via the capacitive gap, and dimensions of the SRRs are tuned to produce a resonant permittivity $\epsilon(\omega)$ [66]. Simultaneously, the H field of incident radiation couples to the structure through the spacer layer between the SRR and the ground plane, producing a permeability $\mu(\omega)$ with the same resonant frequency as $\epsilon(\omega)$. On resonance, the electromagnetic impedance is nearly matched to that of free-space, and reflections from the MM drop to near zero at the resonant frequency ω_0 . The transmittance through the structure is necessarily

zero due to the continuous gold ground plane and a high absorption peak forms near ω_0 . More details on the theory of MM perfect absorbers and some alternative approaches to modeling the absorption properties can be found in Watts et al. [66] Chen et al. [67], and Huang et al. [68].

A perfect absorber can be turned into a saturable absorber by coupling a nonlinear material inclusion to the confined fields inside the resonator elements of the absorber. This causes the absorption to become power dependent, with the peak absorption decreasing as THz power incident on the device increases. Several approaches have been used to make THz saturable absorbers. In Figure 4c,d, we highlight two such approaches. Figure 4c shows the response of a reflecting perfect absorber with an absorption peak designed for 0.45 THz. The nonlinear response arises directly from the SRR array, which is etched out of a superconducting YBCO film [62,69].

Superconductors have long been of interest for tunable and nonlinear MM devices due to their highly nonlinear material properties that can be tuned via a variety of avenues, including via controlling ambient temperature or via externally applied electric and magnetic fields [70–73]. The YBCO film conductivity depends strongly on both ambient temperature and the strength of the incident THz fields [74,75]. As the field strength of the incident THz pulse is increased, the resonant fields in the SRR induce very large localized current densities, which act to quench the superconducting state of the resonator [76]. The increasing effective resistance dampens the resonant response, which disrupts the impedance matching condition in the metamaterial and lowers the peak absorption. At $T = 10$ K, the absorption at the design wavelength saturates from 0.8 to 0.4 as the incident THz pulse field is increased from 40 kV/cm to 200 kV/cm. Although the overall change in peak absorption is smaller at higher temperatures, the saturation response is still measurable for all temperatures below the superconducting transition temperature of the YBCO SRRs. Of course, the main performance limitation for superconductor based saturable absorbers is the low temperature requirement. Even when using a High- T_c material such as YBCO, the transition temperature limits metamaterial functional temperatures to below approximately $T = 90$ K.

Figure 4d shows another example of a THz saturable absorber based on the reflecting perfect absorber design [62]. Notably, this device functions at room temperature conditions and the bulk GaAs substrate is etched away leaving only the MM perfect absorber elements on a flexible polyimide support (see inset of Figure 4d) that can conform to a variety of surfaces [21,77]. A second benefit of this design is the elimination of Fabry-Perot reflections from the absorber. Such reflections are a common limitation on the overall absorption and application of perfect absorbers designed to operate as reflecting elements.

The power dependent absorption in the device from Zhao et al. [63] arises from a small patch of GaAs placed within the SRR gap region. The confined electric fields of the gap induce impact ionization in the GaAs [51,54]. Increased carrier conductivity then dampens the SRR resonance and decreases the absorption peak at the design wavelength of 0.6 THz. Although the saturation response is smaller than in the previous example, the absorption peak still saturates by close to 15% of its value at low field strengths. Many applications of saturable absorbers, in particular active mode-locking techniques, only require a net change in absorption of 1–2%. Coupling THz saturable absorbers as shown here with recent advances in direct THz laser sources, such as quantum cascade lasers [78,79], one can imagine the future possibility of an actively mode-locked THz laser source.

2.4. Field Confinement Applications in Nonlinear Spectroscopy

Beyond nonlinear devices, MM and plasmonic field confinement has also contributed to new techniques in nonlinear THz spectroscopy [80] and we finish the MM section of this review with an overview of recent advances in this field. MM field confinement first made an impact in the study of the correlated electron material VO_2 , where the confined THz fields in a SRR array were used by Liu et al. to excite an insulator to metal transition in an underlying VO_2 film [10]. The confined THz fields lower the overall potential barriers to charge carrier transport, inducing the phase transition. Uniquely, in this study, the MM resonator was also used to probe the phase transition. The VO_2 conductivity increase

results in a large dampening of the MM SRR resonance, clearly seen in spectroscopic measurements and pump-probe data.

It is generally accepted that the insulator to metal transition in VO₂ is driven by electron-electron and electron–lattice interactions [81], but the role of lattice structural changes, while of high interest, is less well-understood [82,83]. Recently, this technique of MM-enhanced THz nonlinear spectroscopy has been extended to probe, on ultrafast timescales, the electronic nature of the VO₂ phase transition simultaneously with the associated structural changes to the crystal lattice. Figure 5a,b highlights this work by Gray et al. [84]. As shown in Figure 5a, a VO₂ film is patterned with long gold bars that act as a resonant MM system. Incident THz pulses are confined to the spaces between the gold bars and reach peak magnitudes of ~2 MV/cm. The confined fields excite the insulator to metal transition in the VO₂ film within the gap regions of the MM structure. An optical pulse is then used to probe the electronic dynamics of the film, while a 7 keV X-ray probe (from the Linac coherent light source at the Stanford Linear Accelerator, Menlo Park, CA, USA) is used to probe the structural dynamics. Gray et al. [84] determined from this measurement that the phase transition is initiated by electronic dynamics, namely THz induced Zener-Keldish tunneling and Wannier-Stark band renormalization. A structural transition, as shown in Figure 5b, from an insulating monoclinic configuration to a metallic rutile phase follows the electronic transition on much slower time scales, and is caused by lattice heating due to currents induced by the confined THz fields.

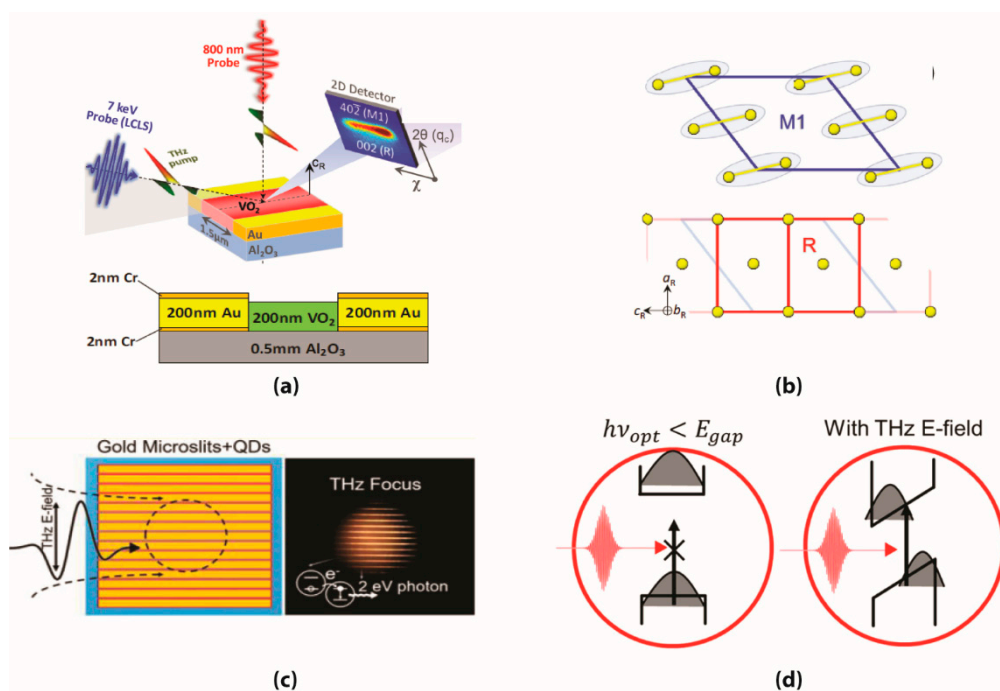


Figure 5. (a) An example of THz fields confined using a MM structure used to excite a phase and structural transition in VO₂. The THz induced structural transition is probed using a 7 keV X-Ray source. Reprinted with permission from [84]. Copyright 2018 by the American Physics Society. (b) The induced structural transition from M1 to R phases probed in (a). (c,d) Confined THz fields used to excite a quantum Stark effect and photoluminescence in Cd-Se quantum dots. Reprinted with permission from [85].

THz FC has also been used to modulate photoluminescence from Cd-Se quantum dot (QD) structures. Electric field modulation of QDs is of interest as a basis for new tunable and actively modulated photonic devices. Active modulation of QDs with external electric fields has been reported previously [86,87], but dielectric breakdown for applied fields of 1–10 MV/cm limits experimental possibilities [85]. Recently, Pein et al. [85] used THz field confinement to overcome this limit. In this paper, gold bar MM antennas similar to those used in Gray et al. [84] are fabricated in a Cd-Se QD

sample to confine incident THz fields to the gap regions between the bars. Figure 5c shows a schematic and photograph of this sample structure. Although the peak confined fields reach ~ 1 MV/cm, the threshold due to dielectric breakdown is significantly higher for THz frequency excitation. Thus, Pein et al. [85] were able to use an incident THz pulse to control QD properties without damaging the device. In particular, they were able to induce photoluminescence in their quantum dot samples solely due to the incident THz excitation. This photoluminescence is due to a THz induced Stark effect that bends the QD bandgap, as illustrated in Figure 5d.

Resonant slot antennas have also paved the way for new studies concerning high-field spectroscopy to induce nonlinear effects [88,89] and applications of FC for enhanced sensing of low-concentration samples. In contrast to dipole antennas and MMs, slot antennas have the advantage that a sample can be confined and measured only in the region where the electric field is enhanced [90], and the measured field enhancement (FE) can simply be estimated from a THz-TDS experiment on the slot antenna sample using

$$FE = \frac{|t(\nu)|}{\beta} \quad (6)$$

where β is the geometric fill factor, i.e., the area of the slot antenna divided by the area exposed by the THz beam for a single slot antenna [91] or the area of the lattice for an array of slot antennas [92]. The field transmission factor, $t(\nu)$, is simply $E_{\text{sample}}/E_{\text{reference}}$ for a free-standing metallic film of slot antennas, while for structure fabricated on a substrate such as typical Si wafer, Fresnel losses from this substrate should be included if referencing to a measurement without any sample in the beam path [92]

$$t(\nu) = \frac{(n_{\text{substrate}} + 1)^2}{4n_{\text{substrate}}} \cdot \frac{E_{\text{sample}}}{E_{\text{reference}}} \quad (7)$$

When applying slot antennas for spectroscopy of samples deposited in to the slots, the high field enhancement also gives a dramatically increased absorption cross section, as illustrated in Figure 6a [93]. Having a single slot antenna resonant around 0.87 THz with a width of 50 nm, the THz absorption cross section is increased more than 10 times, which can be used to detect the presence of the widely used organic explosive (O_2NNCH_2)₃, known commonly as “RDX.” Similar structures have also been used to sense other biomolecules such as pesticides [94] and sugar molecules [95]. Later, by performing an optical pump-THz probe experiment on the structure, the same research group also showed that resonant slot antennas fabricated on semiconductor substrates can reveal new information about the carrier dynamics in the surface layer of the substrate [96]. Here, they reported that the carrier lifetime of the substrate significantly decreases when decreasing the width of the slot antenna altering the carrier lifetime from that measured in the bulk substrate (see Figure 6b). For these structures to achieve nano-sized widths of the slot antennas, advanced fabrication methods such as e-beam or focused ion beam lithography are required. However, it has been shown that array structures can be optimized to achieve additional FC using lattice modes [97,98]. With this, slot antenna arrays with dimensions on the microscale can be optimized and fabricated with standard photolithography, where each slot antenna achieves a FC that is 60% larger than for an isolated slot antenna. As a compliment to the nano-sized structures, this offers an increasing potential for THz sensing with microstructures where lower fabrication cost or the larger width itself is preferred.

As can be seen from the examples outlined above, THz FC has made a large impact on MM research, opening up new avenues for nonlinear devices at THz frequencies and beyond, and providing new applications for MM structures in enhanced sensing and nonlinear studies of ultrafast dynamics. However, this is only part of the story. Concurrently, THz FC has also played a role in the development of novel techniques for sub-wavelength THz near-field imaging. In Section 3, we turn our attention to the remarkable developments that have taken place in this field.

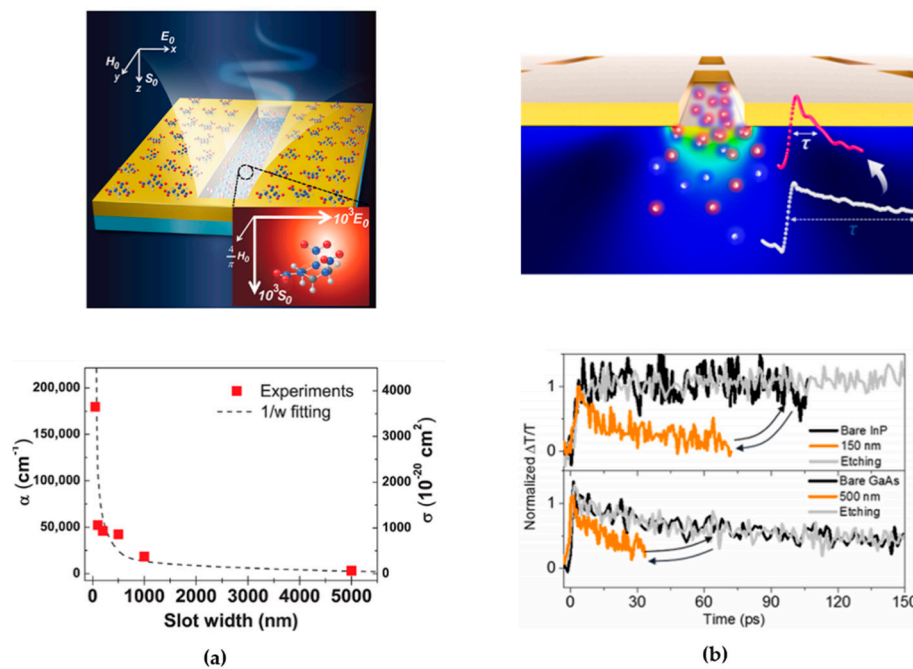


Figure 6. (a) Resonant slot antenna achieving an increased absorption cross section when reducing the slot width on the nanoscale. Reprinted with permission from [93]. (b) Optical pump-THz probe experiment on slot antennas showing reduced carrier life time due to the surface sensitivity of this method. Reprinted with permission from [96].

3. Field Confinement for Sub-Wavelength Imaging at Terahertz Frequencies

3.1. Early Work in Sub-Wavelength THz Imaging

Sub-wavelength imaging has been of much interest in the THz community during the past decades since diffraction limits the spatial resolution of conventional THz systems to the order of hundreds of microns [99]. Given interest in using THz beams for studies of subwavelength structures such as MMs, integrated circuits, and biomolecules, this diffraction-limited resolution is far from sufficient [100].

Most approaches for sub-wavelength THz imaging are based on scanning near-field optical microscopy (SNOM) probes, which take advantage of FC of the THz beam at the apex of the probe to increase the spatial resolution. One of the first examples of this idea was reported by Hunsche et al. [101] using a standard THz spectrometer in combination with a tapered metal tip, as shown in Figure 7a. By scanning a test sample of subwavelength apertures, as shown in Figure 7b, they observed a spatial imaging resolution of 50 μm using THz pulses with an average wavelength of 220 μm , a resolution of $\lambda/4.4$. Similarly, FC with tapered waveguides and apertures was later demonstrated [102–106] yielding a “superfocus” of the size $\sim \lambda/260$ at 0.1 THz [107]. The concept of tapered waveguides has also been used in combination with intense ($\sim \mu\text{J}$) THz pulses generated from amplified laser systems with kHz repetition rates [108,109]. The robustness of the tapered waveguides allows for simple manufacturing and material degradation, similar to that shown in Figure 1d, of the tapered material is less likely to happen. More sophisticated versions of tapered apertures for THz imaging have also been proposed, such as a metal-coated dielectric waveguide yielding a spatial resolution of 40 μm [110] or a tapered fiber consisting of a metallic wire array reaching $\lambda/28$ for the lowest frequencies around 75 GHz in a standard THz time-domain spectrometer [111].

Similar to tapered waveguides and apertures, tapered versions of standard photoconductive antennas (PCA) are also possible, offering near-field detection with a spatial resolution down to 5 μm [112]. Today, similar tapered PCAs are commercially available (Protometrics GmbH).

3.2. THz Imaging with s-SNOM

Although the tapered apertures are an intuitive and simple solution that has moved the field of THz imaging from the mm- to the μm -scale, it is practically challenging to handle tapers at the sub- μm level. Additionally, theoretical considerations suggest that tapered waveguides, even in the most ideal of cases, are limited to resolutions near a few hundred nm [113]. Instead, “apertureless” SNOM techniques have successfully pushed optical microscopy to the nanoscale [114–120], which was first demonstrated for microwaves [121] and mid-IR light [122]. In 2003, SNOM with THz pulses was for the first time demonstrated by Hou-Tong Chen and co-workers, as shown in Figure 7c, who achieved a spatial resolution of 150 nm by imaging a silicon-gold grating (Figure 7d) [123]. Here, a metallic probe with a sharp tip serves as the near-field probe both due to the plasmonic FC below the tip and the tip’s ability to elastically scatter light off its subwavelength volume [124]. For this reason, this method is often referred to as scattering-type SNOM (s-SNOM). s-SNOM shows superior spatial resolution for non-contact optical imaging of samples with sufficiently high dielectric functions to obtain a scattered signal from a sub-wavelength volume. However, a major challenge in s-SNOM measurements is that typically most scattered light originates from places other than the region directly below the probe. Lock-in detection can efficiently suppress this background scattering, through oscillating the probe tip above the sample surface and locking to a harmonic of the oscillation frequency. The higher the harmonic is, the better are the background suppression and sensitivity to the near-field confined just below the tip and, ideally, the higher is the spatial image resolution. However, the trade-off is that the total measured signal strength decreases [125].

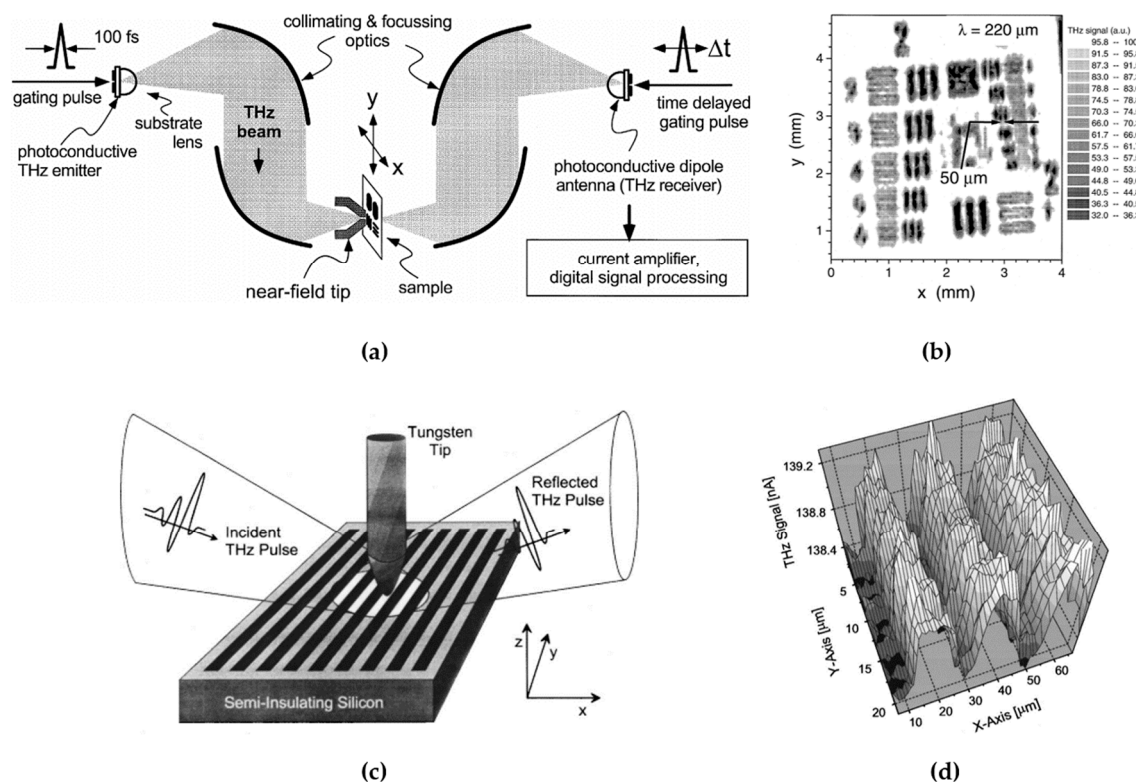


Figure 7. Early work of sub-wavelength THz imaging: (a) Imaging setup using a tapered metal tip and (b) the measured test sample showing 50 μm resolution at 220 μm . Reprinted with permission from [101]. (c) THz SNOM setup for imaging of a silicon-gold grating and (d) the resulting image with a spatial resolution of 150 nm. Reprinted with permission from [123].

The more complex out-of-plane geometry of the s-SNOM setup coupling light from an angle to the tip of the metallic near-field probe means that the field enhancement at the tip is difficult to estimate. Typically, this is done with finite-element simulations, as shown in Figure 8. However, simulating the

actual experimental conditions can be difficult. Often, it is unknown how large the actual tip diameter is, if the tip is contaminated, or the exact angle of incident light. Nevertheless, since the goal in most cases is to achieve a high image resolution, this is in practice measured by scanning over a sharp edge and comparing the line-scans of the AFM signal and the near-field signal. The field confinement can be estimated by approaching the tip to the surface and measuring the exponential increase of the scattered signal. Here, the $1/e$ -width of this signal is typically referred to as the field confinement of the field below the tip.

A key element of the s-SNOM techniques is that the tip not only confines and scatters the incident light, but also facilitates interaction of the light's with the sample below the tip. The simplest model to describe this is the "Point-dipole model" considering the tip as a small polarizable sphere [125], while the more complex "Finite-dipole model" approximates the tip with a spheroid taking the elongated shape of the tip in to account [126]. This has later been used to further develop an analytical model for extracting material parameters such the dielectric permittivity from an s-SNOM experiment using a mid-IR light source with interferometric detection [127].

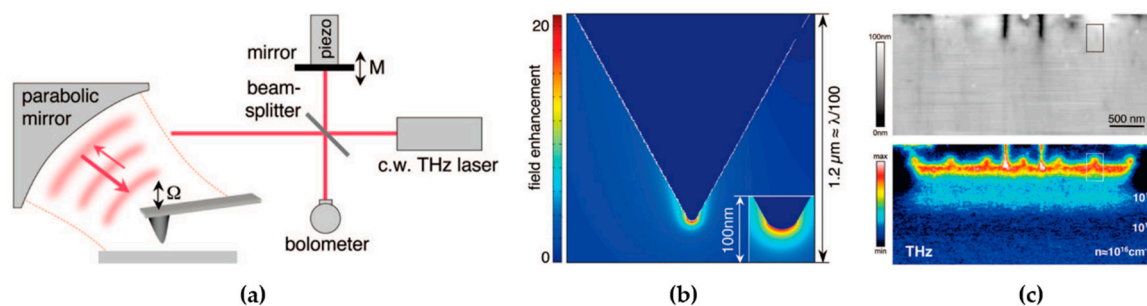


Figure 8. (a) s-SNOM setup using a THz CW laser at 2.54 THz; (b) electro-dynamical simulations of the FC for a standard AFM probe; and (c) the resulting AFM and THz image. Reprinted with permission from [128].

3.3. s-SNOM with CW and Pulsed THz Sources

For nanoscale imaging with continuous wave THz lasers at 2.54 THz, the technology of tapping-mode atomic force microscope (AFM) was adopted and combined with a well-engineered parabolic mirror system for both coupling light to and collecting scattered light from the tip (see Figure 8a). Here, Huber et al. performed electro-dynamical simulations to estimate the FC for a standard AFM probe used in this experimental configuration [128]. Field enhancements of up to 25 times were estimated in a radius of 30 nm at the tip of the probes (see Figure 8b). Using this FC, a sample of semiconductor transistors was imaged both with the AFM and THz nanoscopy methods (Figure 8c) as well as a mid-IR source with a wavelength of 11 μm for comparison (not shown here). While the AFM image showed an almost flat topography with no clear features, the THz nanoscopy image clearly resolved the seven transistors horizontally aligned in the top of the image. Here, the image resolution was 40 nm, significantly better than seen for other THz imaging near-field methods. Furthermore, the THz image also showed a contrast related to varying carrier concentration which did not appear in the mid-IR image for the same sample. This contrast is seen in the lower image of Figure 8c. The lighter blue region corresponds to a carrier concentration of $\sim 10^{18} \text{ cm}^{-3}$ while the darker blue region corresponds to a carrier concentration of $\sim 10^{16} \text{ cm}^{-3}$.

Since the manifestation of s-SNOM for THz nanoscopy, several results reporting new features in this regime have been published. Similar to the work presented by Huber and co-workers [128], reports using THz CW sources have shown new potential for studying THz frequency phenomena on the nanoscale [129–131]. For example, Degl’Innocenti et al. [131] demonstrated a compact solution for THz nanoscopy using a QCL as both a source and a detector in combination with an s-SNOM system. With this system, they performed imaging at 2.85 THz of a metallic photonic crystal structure with a plasmonic resonance at the imaging frequency, achieving a spatial resolution of 78 nm. Another recent

study by Liewald et al. [130] presents a tunable CW option for nanoscopy from 0.5 to 0.75 THz. Here, the authors used the 54th harmonic of a synthesized microwave source as both the tunable THz source coupled to the s-SNOM system and a heterodyne detection of the back-scattered THz beam. With this microwave-based THz transceiver, the system offers “all-electronic control” of the s-SNOM including tunability of the THz imaging frequency.

THz s-SNOM has also been performed at the free-electron laser facility FELBE in Dresden, Germany [132,133], offering high power signals with broadband tunability. Here, the facility offers powers up to 10 W in a tunable range from 1.3 to 75 THz. With such high powers and tunability, the s-SNOM at FELBE offers spectrally resolved nanoscopy that is, at the moment, hard to obtain with the table-top systems discussed above. With this, THz nanoscopy has been performed up to 8.5 THz on gold nanostructures [132], where the imaging results are shown in Figure 9a–f. The AFM topography in Figure 9a shows a mixture of connected and isolated gold islands, and, while the s-SNOM image recorded at 1.3 THz referenced to the 2nd harmonic of the cantilever oscillation still contains some background signal from far-field radiation (Figure 9b), the 3rd harmonic signal is free from any background (Figure 9c). When observing an isolated and a connected gold region indicated as A and B, respectively, in a zoomed region (Figure 9d), the near-field of the connected region is much larger than for an isolated region as seen in (Figure 9e), which is due to the larger polarizability of the connected gold regions. For the brightest regions in the near-field image recorded at the 3rd harmonic, the spatial resolution was estimated to be 50 nm (Figure 9f).

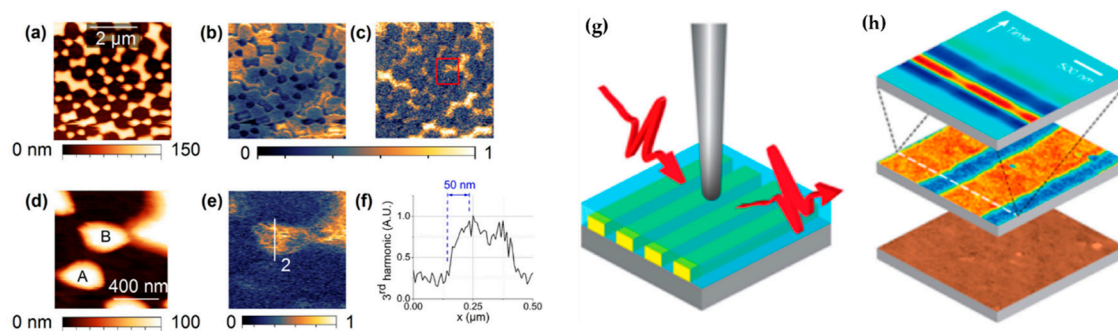


Figure 9. s-SNOM images of gold islands measured with a free-electron laser at 1.3 THz: (a) AFM topography; (b) near-field image referenced to the 2nd harmonic; and (c) the 3rd harmonic. (d) AFM topography and (e) the 3rd harmonic near-field image of the zoomed region indicated in (d). (f) Line scan over the gold structure indicated in (e). Reprinted with permission from [132]. (g) Illustration of THz s-SNOM imaging of the embedded gold grating and (h) the resulting images of AFM topography, THz peak field image and corresponding waveforms along the white line (bottom to top). Reprinted with permission from [134].

Except for the first demonstration of SNOM in the THz range by Chen et al. [123], the nanoscopy experiments discussed above have all been carried out with CW THz sources. Nevertheless, several studies have also been published using pulsed THz sources [135–138], making possible nanoscopy measurements in time-domain [134,139]. With such a time-domain THz s-SNOM system, Moon et al. performed spatiotemporal imaging with a spatial resolution of 90 nm of a sub-wavelength grating structure (Figure 9g,h) [134]. Furthermore, they demonstrated that the gold grating structure could be measured, even though it was embedded in a dielectric film with a topographically flat surface (bottom layer in Figure 9h). For THz nanoscopy measurements, they found that the THz probe near-field was well-confined for the first harmonic of the demodulation frequency and did not improve significantly when referencing to the 2nd or 3rd harmonic. However, the 1st harmonic was much more sensitive to subsurface structure than the higher harmonics. This is in agreement with what has been observed in the mid-IR [140,141].

3.4. Variations of s-SNOM Configuration for THz Imaging

In addition to the conventional s-SNOM configurations used with a direct THz source, new variations of the technique have also been published. For example, Alonso-González et al. recently developed photocurrent nanoscopy, where the near-field under the AFM probe is measured directly by a graphene-based device [142]. While the experiment discussed here was carried out with a CO₂ laser ranging from 2.52 to 5.67 THz, the same groups also demonstrated photocurrent nanoscopy with light sources in the infrared [143,144]. The graphene-based device heterostructure consists of a graphene layer encapsulated in two layers of hexagonal boron nitride (h-BN), which is placed on top of two gold electrodes (LG1 and LG2) capable of controlling the carrier concentrations, creating a sharp p-n junction in the graphene above the electrodes. The THz near-field is detected by a photothermoelectric effect in the graphene sheet. A local temperature gradient generated by the THz near-fields, producing a net electric current which is sensitive to the change in carrier concentration in the p-n junction. This net current is measured at the contacts fabricated on the sides of the heterostructure and referenced to the oscillation of the tip in a similar way as for an s-SNOM experiment. Figure 10b shows the photocurrent induced by the THz near-field at 2.52 THz where the spatial resolution was estimated to be 50 nm. As expected, the photocurrent was found to be highest in the center of the sample at the junction. Furthermore, the vertical oscillations in the photocurrent were attributed to THz induced graphene plasmons at the interface of the graphene layer and the upper layer of h-BN. The photocurrent oscillations were measured along the white dashed line for four different frequencies from 2.52 to 5.67 THz (Figure 10c). From these, the plasmon wavelengths were extracted and plotted as the red dots in Figure 10d. Interestingly, a linear dispersion is observed at low frequencies, which is in contrast to what typically is observed for free-standing graphene (solid blue line), thus the oscillating photocurrent for the heterostructure is attributed to acoustic plasmons. The images in this experiment also revealed that these acoustic plasmons were much more confined than for free-standing graphene yielding wavelengths approximately 12 times smaller. The direct electrical mapping of the optical THz near-field with such graphene-based structure with a linear dispersion is therefore a promising method for mapping photocurrents on the nanoscale.

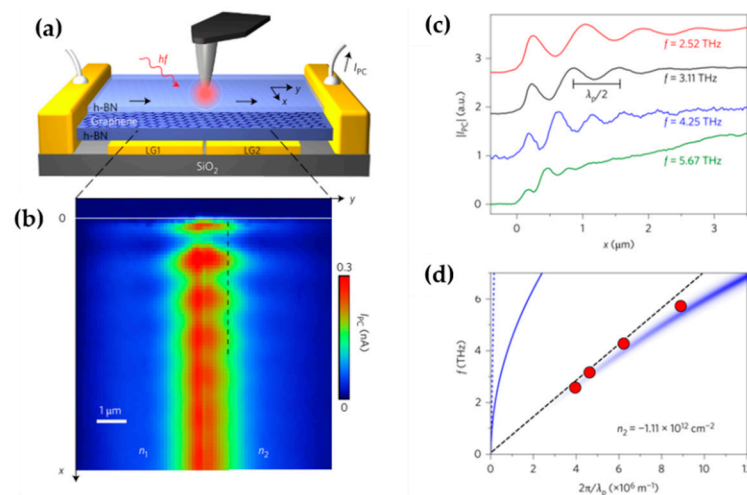


Figure 10. THz photocurrent nanoscopy: (a) Illustration of the experimental setup. LG1 and LG2 represent the split gates of gold used to control the carrier concentration in the graphene. (b) Photocurrent image recorded for 2.52 THz and with $n_1 = 0.77 \times 10^{12} \text{ cm}^{-2}$ and $n_2 = -0.71 \times 10^{12} \text{ cm}^{-2}$ set by LG1 and LG2, respectively. (c) Near-field photocurrent profiles for different frequencies recorded along the dashed line in (b,d) Experimental (red dots) and theoretical dispersion relations in the heterostructure (blue color plot), free-standing graphene (blue solid line), light line in free space (blue dashed line), and acoustic plasmons (dashed black curve). Reprinted with permission from [142].

Another technique for subwavelength imaging is Laser THz Emission Microscopy (LTEM) that relies on the fact that most semiconductors can intrinsically, or by applying an external bias, emit THz pulses when being photo-excited by fs laser pulses. Since these typically have wavelengths in the NIR, they can be focused to a diffraction-limited spot much smaller than THz frequency pulses, giving an improved imaging resolution by more than two orders of magnitude [145]. For example, integrated circuits have been imaged with a spatial resolution down to 1 μm [146], but the method has also been used to study physical processes in THz radiating materials [147–152] or processes on the surface of the radiating semiconductor [153–155]. Recently, the spatial resolution of LTEM was improved even further by implementing it in an s-SNOM microscope where a gold nanorod was imaged on a THz radiating InAs substrate (Figure 11) [156]. Here, the spatial resolution was estimated to be similar to the simultaneously recorded AFM image of approximately 20 nm.

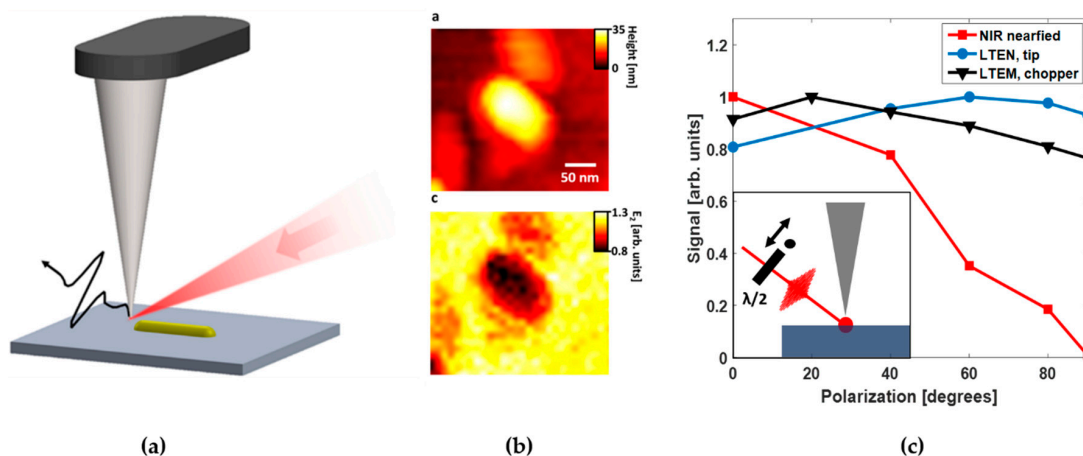


Figure 11. (a) Illustration of nanoscale LTEM (Laser THz Emission Microscopy); (b) AFM and nanoscale LTEM image referenced at the 2nd harmonic; and (c) polarization dependent signals of nanoscale LTEM signal (blue), the NIR near-field signal (red) and the LTEM signal referenced to an optical chopper when turning the polarization of the incident NIR beam as illustrated in the inset. Reprinted with permission from [156].

Perhaps the most intuitive way to visualize this nanoscale LTEM experiment is to assume that a NIR near-field below the apex of the tip generates a THz signal from a nanoscopic volume in the sample whenever the oscillating tip is in close proximity of the sample. However, this explanation was ruled out by experiments that varied the polarization of the incident NIR beam relative to the probe tip. The red curve in Figure 11c shows that the NIR near-field signal dropped to zero when the polarization was turned from vertical to horizontal, as defined in the inset of Figure 11c. Interestingly, the THz near-field signal remained and even increased slightly. This increase suggests that the NIR near-field screens the THz signal. Additionally, it is well-known that the THz radiation from InAs has a minor dependence on the polarization of the incident beam due to the crystal orientation of the surface [157]. This was illustrated by a subsequent measurement where the LTEM signal is referenced to an optical chopper rather than the oscillation of the tip. This experiment showed that the nano-resolved LTEM signal is relatively independent of the NIR near-field signal. It was concluded that the tip acts as a nanoprobe, discriminating the THz radiation coming from a nanoscale region from a larger volume determined by the spot size of the incident NIR laser beam ($\sim 10 \mu\text{m}$). It was possible to map areas screening the THz radiation with a spatial resolution on the nanoscale such as the gold structure seen above in Figure 11b. The method has a solid potential for imaging samples where the carrier mobility varies on the nanoscale including nanowires, carbon nanotubes and other semiconducting nanostructures. With the single NIR beam incident on the sample, the nanoscale LTEM technique offers a much simpler imaging configuration than nanoscale pump-probe experiments with s-SNOM, which have been carried out with mid-IR probe pulses [141,158].

3.5. AFM Probes for THz Nanoscopy

A technical challenge of using the s-SNOM technique in the THz range is that the measured signal critically relies on the dimensions of the tip. Obviously, the shank of the tip should be tapered down to a diameter of similar size as the desired spatial resolution, but the length of the tip also plays an important role, providing a resonance effect that enhances the detected signal [135,159–161]. In the THz range, this favors tips with lengths on the order of 100 μm to reach a $\lambda/2$ resonance. With a taper down to around 10 nm, such tips are both challenging to fabricate and fragile to use. A limited selection of commercial nanoprobes with lengths around 80 nm and tip apex radii down to 10 nm are available (Rocky Mountain Nanotechnology, Salt Lake City, UT, USA), and a thorough study of custom fabricated probes in the THz range was recently reported by Mastel et al. [160]. Here, six different lengths of tips from 17 to 78 μm were fabricated in an 80/20 Pt/It alloy, all with a tip apex diameter of 50 ± 3 nm. The near-field intensity at the tip apex for each length was studied in an s-SNOM setup with a CW laser at 3.11 THz (96.5 μm). The near-field signal is measured with the same THz graphene detector and photocurrent technique shown above in Figure 10. In Figure 12a, the measured photocurrents corresponding to the THz near-field for each tip length (blue dots) correlate well with numerical full-wave simulations performed for similar tip and sample structures with varying lengths (blue solid line). The simulations and experiments combined reveal that the two maxima correspond to the first ($\sim\lambda/2$) and second order ($\sim\lambda$) antenna resonances, although the position of these resonances are slightly lower than the theoretical value for the considered wavelength. This shift is related to the presence of the cantilever and the sample was studied further in Figure 12b. Simulated resonances for different configurations of the sample, tip, and cantilever system were compared to the resonance for an isolated tip (A). Here, it was observed that redshift of the antenna resonance peak depended only on the presence of the cantilever (B), while the presence of the sample only enhanced the resonances (C and D). Further simulations studied the effect of the graphene layer below the 9 nm hBN layer (C) on the tip resonance. This result was then compared to a simulation where the graphene layer in the sample was replayed by a Perfect Electric Conductor (PEC, D). Interestingly the PEC layer only results in only a slightly higher field enhancement ($\sim 20\%$) than the graphene layer, suggesting that the graphene layer acts similar to a PEC in the near-field of the tip.

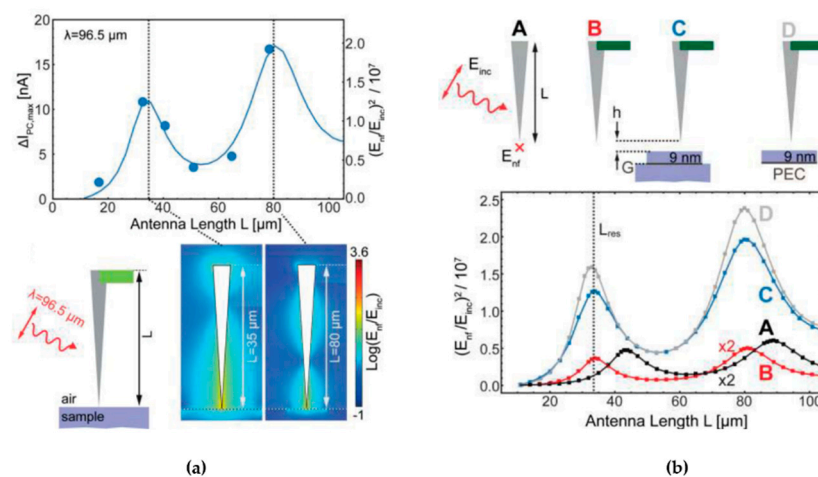


Figure 12. Resonant THz probes: (a) Measured THz near-field induced photocurrent as a function of antenna length (blue dots) together with full-wave simulation of the illustrated structure. The resulting simulations of the two resonances marked as the dotted black lines are shown below the plot. (b) Illustration and resulting field enhancements 10 nm below the apex as a function of length for four configurations: (A) free-standing tip; (B) tip with a cantilever; (C) tip with cantilever and graphene-based device as described in the text; and (D) tip with cantilever and sample device where graphene has been replaced by PEC. Reprinted with permission from [160].

3.6. Evolution of Sub-Wavelength THz Imaging

Overall, the study by Mastel and co-workers emphasizes the advantages of using resonant tips for s-SNOM, and technological progress in the fabrication of even longer metallic nanoprobes could offer even better imaging contrast at the lower frequencies in the THz range. From all the examples discussed above, it is clear that the usage of metallic tips in s-SNOM configurations or variations thereof has already revolutionized THz imaging, yielding now more than four orders of magnitude improvement in resolution. To emphasize this progress, we have collected in Figure 13 a selection of reports of imaging techniques that beat the diffraction limit and plotted improved spatial image resolution over time. The improvement of the diffraction limit is calculated as the image wavelength divided by the achieved spatial resolution. For experiments where standard PCAs are used as THz sources and detectors, the weighted mean wavelength is approximated to 299 μm (1 THz). All the tip-based approaches are collected under the name “Apertureless” adopted from the early reports using tips for near-field imaging [118,162]. In Figure 13, we see how the initial work on sub-wavelength imaging was driven by methods such as tapered apertures or waveguides [101,107,110]. LTEM [146] and near-field detection methods [112,163–166] moved THz imaging to the microscale, and the further push down to the nanoscale came with the implementation of the tip-based approaches in THz imaging systems [123,128,134,167,168]. For the sake of comparison, we have also included apertureless imaging reports in the mid-IR [141,169,170] and MW [121] as well as the stimulated emission depletion microscopy (STED), which first was developed by Hell and co-workers in 1994 [171], and for which the Nobel Prize in Chemistry was awarded in 2014. When strictly speaking about beating the diffraction limit or “super-resolution imaging”, the impressive mid-IR s-SNOM imaging results reaching 5 nm of spatial resolution using ultrasharp Tungsten tips with a diameter of 6 nm [170] still lie below the THz s-SNOM results due to the longer wavelengths of THz light. On the other hand, the first MW s-SNOM result by Knoll and Keilmann with its GHz light source [121] is by far superior to all other results discussed here.

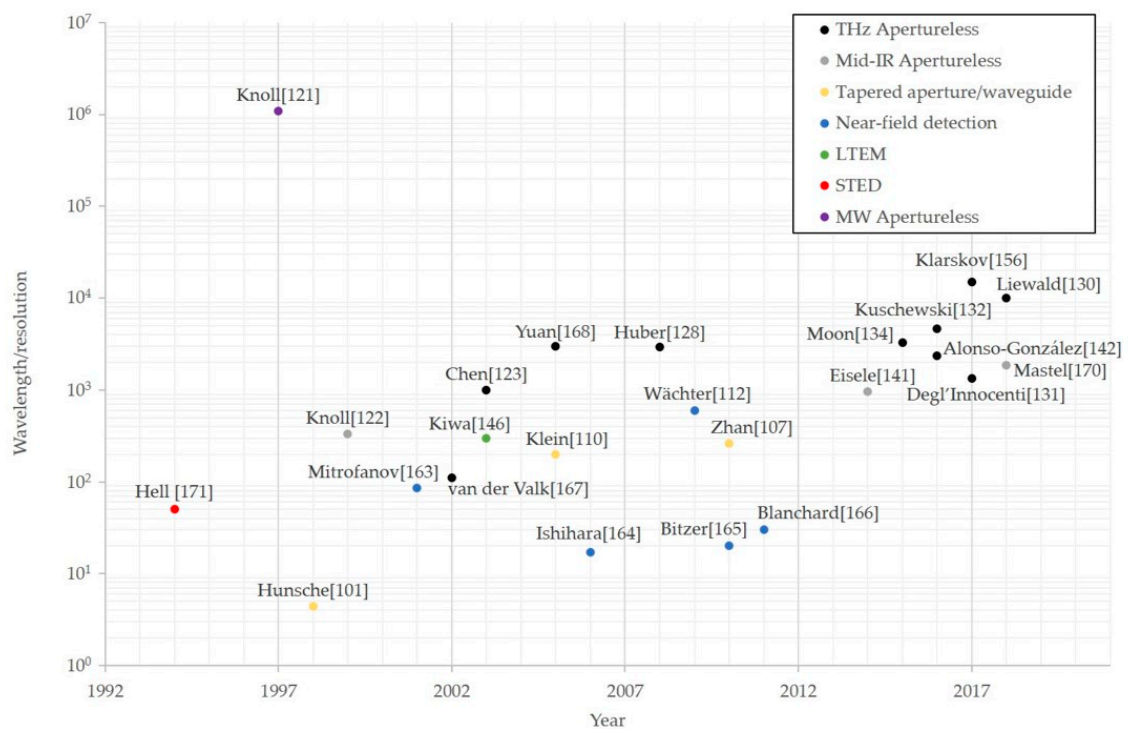


Figure 13. The development of sub-wavelength imaging methods over time.

4. Discussion and Conclusions

The works reviewed above constitute a brief summary of recent developments in two areas of THz science and engineering: nonlinear metamaterial devices and high-resolution near field nanoscopy. In particular, we highlight the central role played in this research by novel methods of controlling THz field distributions, in particular devices and techniques for confining THz fields on the microscopic and nanoscopic scales.

These results comprise only a subset of the impressive progress made in recent years in the field of THz photonics engineering. Of course, challenges in both nonlinear metamaterial devices and near-field nanoscopy remain. One significant challenge for nonlinear THz MMs is in the design of non-resonant nonlinear devices. Nonlinear THz MMs based on FC techniques have been, to date, dependent on an underlying resonant nonlinearity in the substrate material. Resonant nonlinearities inherently involve exciting electronic state transitions in the underlying substrate, and lend themselves well to effects such as saturable absorption. Thus, as shown above, the development of nonlinear absorbers via SRR field confinement has been exceptional. However, the design of nonlinear THz metamaterials exhibiting non-resonant nonlinear effects, such as a pure $\chi^{(3)}$ response, has not seen nearly as much progress as similar lower frequency devices [40].

For sub-wavelength THz near-field imaging, nanoscale pixel sizes have been achieved using the s-SNOM techniques, where the spatial resolution scales with the size of the tip apex. With commercially available nanoprobe for THz imaging, and new impressive results yielding 5 nm resolution for mid-IR s-SNOM using custom Tungsten tips, it could be plausible to expect THz imaging resolution to continue down towards the Ångström level with the development of sharper tips. A main challenge in the THz range is to downscale the tip apex while keeping the resonant geometry unchanged. This means that the tip shank lengths still need to reach around 100 μm , while the tip apex is much thinner. While challenging, fabricating such tips might be possible. For instance, Pt/Ir alloys have shown to significantly improve the robustness and strength near-field probes compared to pure Pt. Other alloys or materials might also have potential for improving the robustness of the near-field probe itself as well as providing a higher field enhancement due to improved material properties and tailored geometry.

However, the downscaling of pixel sizes also calls for more sensitive methods than THz photocurrent nanoscopy for detecting THz signals in the far-field or directly in the near-field. Much work is currently being done on improving THz emitters and detectors, and this will surely impact the future high-resolution THz imaging systems, for both a better contrast and faster image recording.

To conclude, we believe these results highlight exceptionally well just how far the THz field has progressed. In only a few decades, the THz gap, to great extent, has been filled, and the field has now moved into new realms previously thought inaccessible to THz science. As THz science continues to progress, we expect even more exciting results in the not too far future. While the THz electric fields in the above results are quite tightly confined, the possibilities for THz photonics are surely not!

Author Contributions: Both authors contributed equally to this review. Writing, Section 2, G.R.K.; writing, Section 3, P.K.

Funding: This research was funded by the Washington College Faculty Enhancement Fund and Aarhus University Research Foundation (AUFF).

Conflicts of Interest: The authors declare no conflict of interest.

References

1. Sitori, C. Applied physics: Bridge for the terahertz gap. *Nature* **2002**, *417*, 132. [[CrossRef](#)] [[PubMed](#)]
2. Mittleman, D.M. Perspective: Terahertz science and technology. *J. Appl. Phys.* **2017**, *122*, 230901. [[CrossRef](#)]
3. Ma, J.; Shrestha, R.; Moeller, L.; Mittleman, D.M. Invited Article: Channel performance for indoor and outdoor terahertz wireless links. *APL Photonics* **2018**, *3*, 051601. [[CrossRef](#)]
4. Yeh, K.; Hoffmann, M.; Hebling, J.; Nelson, K.A. Generation of 10 J ultrashort terahertz pulses by optical rectification. *Appl. Phys. Lett.* **2007**, *90*, 171121. [[CrossRef](#)]

5. Hirori, H.; Doi, A.; Blanchard, F.; Tanaka, K. Single-cycle terahertz pulses with amplitudes exceeding 1 MV/cm generated by optical rectification in LiNbO₃. *Appl. Phys. Lett.* **2011**, *98*, 091106. [[CrossRef](#)]
6. Hebling, J.; Yeh, K.-L.; Hoffmann, M.C.; Nelson, K.A. High-Power THz Generation, THz Nonlinear Optics, and THz Nonlinear Spectroscopy. *IEEE J. Sel. Top. Quantum Electron.* **2008**, *14*, 345–353. [[CrossRef](#)]
7. Cook, D.J.; Hochstrasser, R.M. Intense terahertz pulses by four-wave rectification in air. *Opt. Lett.* **2000**, *25*, 1210–1212. [[CrossRef](#)] [[PubMed](#)]
8. Jepsen, P.U.; Cooke, D.G.; Koch, M. Terahertz spectroscopy and imaging—Modern techniques and applications. *Laser Photonics Rev.* **2011**, *5*, 124–166. [[CrossRef](#)]
9. Merbold, H.; Bitzer, A.; Feurer, T. Second harmonic generation based on strong field enhancement in nanostructured THz materials. *Opt. Express* **2011**, *19*, 7262–7273. [[CrossRef](#)] [[PubMed](#)]
10. Liu, M.; Hwang, H.Y.; Tao, H.; Strikwerda, A.C.; Fan, K.; Keiser, G.R.; Sternbach, A.J.; West, K.G.; Kittiwatanakul, S.; Lu, J.; et al. Terahertz-field-induced insulator-to-metal transition in vanadium dioxide metamaterial. *Nature* **2012**, *487*, 345–348. [[CrossRef](#)] [[PubMed](#)]
11. Herink, G.; Wimmer, L.; Ropers, C. Field emission at terahertz frequencies: AC-tunneling and ultrafast carrier dynamics. *New J. Phys.* **2014**, *16*, 123005. [[CrossRef](#)]
12. Cocker, T.L.; Jelic, V.; Gupta, M.; Molesky, S.J.; Burgess, J.A.J.; Reyes, G.D.L.; Titova, L.V.; Tsui, Y.Y.; Freeman, M.R.; Hegmann, F.A. An ultrafast terahertz scanning tunnelling microscope. *Nat. Photonics* **2013**, *7*, 620–625. [[CrossRef](#)]
13. Jelic, V.; Iwaszczuk, K.; Nguyen, P.H.; Rathje, C.; Hornig, G.J.; Sharum, H.M.; Hoffman, J.R.; Freeman, M.R.; Hegmann, F.A. Ultrafast terahertz control of extreme tunnel currents through single atoms on a silicon surface. *Nat. Phys.* **2017**, *13*, 591–598. [[CrossRef](#)]
14. Cocker, T.L.; Peller, D.; Yu, P.; Repp, J.; Huber, R. Tracking the ultrafast motion of a single molecule by femtosecond orbital imaging. *Nature* **2016**, *539*, 263–267. [[CrossRef](#)] [[PubMed](#)]
15. Pendry, J.B.; Holden, A.J.; Robbins, D.J.; Stewart, W.J. Magnetism from conductors and enhanced nonlinear phenomena. *IEEE Trans. Microw. Theory Tech.* **1999**, *47*, 2075–2084. [[CrossRef](#)]
16. Pendry, J.B. Negative Refraction Makes a Perfect Lens. *Phys. Rev. Lett.* **2000**, *85*, 3966–3969. [[CrossRef](#)] [[PubMed](#)]
17. Smith, D.R.; Padilla, W.J.; Vier, D.C.; Nemat-Nasser, S.C.; Schultz, S. Composite Medium with Simultaneously Negative Permeability and Permittivity. *Phys. Rev. Lett.* **2000**, *84*, 4184–4187. [[CrossRef](#)] [[PubMed](#)]
18. Schurig, D.; Mock, J.J.; Justice, B.J.; Cummer, S.A.; Pendry, J.B.; Starr, A.F.; Smith, D.R. Metamaterial Electromagnetic Cloak at Microwave Frequencies. *Science* **2006**, *314*, 977–980. [[CrossRef](#)] [[PubMed](#)]
19. Driscoll, T.; Kim, H.-T.; Chae, B.-G.; Kim, B.-J.; Lee, Y.-W.; Jokerst, N.M.; Palit, S.; Smith, D.R.; Di Ventra, M.; Basov, D.N. Memory Metamaterials. *Science* **2009**, *325*, 1518–1521. [[CrossRef](#)] [[PubMed](#)]
20. Landy, N.I.; Sajuyigbe, S.; Mock, J.J.; Smith, D.R.; Padilla, W.J. Perfect Metamaterial Absorber. *Phys. Rev. Lett.* **2008**, *100*, 207402. [[CrossRef](#)] [[PubMed](#)]
21. Tao, H.; Bingham, C.M.; Strikwerda, A.C.; Pilon, D.; Shrekenhamer, D.; Landy, N.I.; Fan, K.; Zhang, X.; Padilla, W.J.; Averitt, R.D. Highly flexible wide angle of incidence terahertz metamaterial absorber: Design, fabrication, and characterization. *Phys. Rev. B* **2008**, *78*, 241103. [[CrossRef](#)]
22. Tao, H.; Strikwerda, A.C.; Fan, K.; Padilla, W.J.; Zhang, X.; Averitt, R.D. Reconfigurable Terahertz Metamaterials. *Phys. Rev. Lett.* **2009**, *103*, 147401. [[CrossRef](#)] [[PubMed](#)]
23. Strikwerda, A.C.; Zalkovskij, M.; Lund Lorenzen, D.; Krabbe, A.; Lavrinenko, A.V.; Uhd Jepsen, P. Metamaterial composite bandpass filter with an ultra-broadband rejection bandwidth of up to 240 terahertz. *Appl. Phys. Lett.* **2014**, *104*, 191103. [[CrossRef](#)]
24. Strikwerda, A.C.; Fan, K.; Tao, H.; Pilon, D.V.; Zhang, X.; Averitt, R.D. Comparison of birefringent electric-split-ring resonator and meanderline structures as quarter-wave plates at terahertz frequencies. *Opt. Express* **2009**, *17*, 136–149. [[CrossRef](#)] [[PubMed](#)]
25. Karl, N.; Reichel, K.; Chen, H.-T.; Taylor, A.J.; Brener, I.; Benz, A.; Reno, J.L.; Mendis, R.; Mittleman, D.M. An electrically driven terahertz metamaterial diffractive modulator with more than 20 dB of dynamic range. *Appl. Phys. Lett.* **2014**, *104*, 091115. [[CrossRef](#)]
26. Chen, H.-T.; Padilla, W.J.; Cich, M.J.; Azad, A.K.; Averitt, R.D.; Taylor, A.J. A metamaterial solid-state terahertz phase modulator. *Nat. Photonics* **2009**, *3*, 148–151. [[CrossRef](#)]

27. Marques, R.; Mesa, F.; Martel, J.; Medina, F. Comparative analysis of edge- and broadside-coupled split ring resonators for metamaterial design-theory and experiments. *IEEE Trans. Antennas Propag.* **2003**, *51*, 2572–2581. [[CrossRef](#)]
28. Zhou, L.; Chui, S.T. Eigenmodes of metallic ring systems: A rigorous approach. *Phys. Rev. B* **2006**, *74*, 035419. [[CrossRef](#)]
29. Strikwerda, A.C.; Zalkovskij, M.; Iwaszczuk, K.; Lorenzen, D.L.; Jepsen, P.U. Permanently reconfigured metamaterials due to terahertz induced mass transfer of gold. *Opt. Express* **2015**, *23*, 11586–11599. [[CrossRef](#)] [[PubMed](#)]
30. Werley, C.A.; Fan, K.; Strikwerda, A.C.; Teo, S.M.; Zhang, X.; Averitt, R.D.; Nelson, K.A. Time-resolved imaging of near-fields in THz antennas and direct quantitative measurement of field enhancements. *Opt. Express* **2012**, *20*, 8551–8567. [[CrossRef](#)] [[PubMed](#)]
31. Zhang, J.; Zhao, X.; Fan, K.; Wang, X.; Zhang, G.-F.; Geng, K.; Zhang, X.; Averitt, R.D. Terahertz radiation-induced sub-cycle field electron emission across a split-gap dipole antenna. *Appl. Phys. Lett.* **2015**, *107*, 231101. [[CrossRef](#)]
32. Chen, H.-T.; O'Hara, J.F.; Taylor, A.J.; Averitt, R.D.; Highstrete, C.; Lee, M.; Padilla, W.J. Complementary planar terahertz metamaterials. *Opt. Express* **2007**, *15*, 1084–1095. [[CrossRef](#)] [[PubMed](#)]
33. Chen, H.-T.; Padilla, W.J.; Zide, J.M.O.; Gossard, A.C.; Taylor, A.J.; Averitt, R.D. Active terahertz metamaterial devices. *Nature* **2006**, *444*, 597–600. [[CrossRef](#)] [[PubMed](#)]
34. Fu, Y.H.; Liu, A.Q.; Zhu, W.M.; Zhang, X.M.; Tsai, D.P.; Zhang, J.B.; Mei, T.; Tao, J.F.; Guo, H.C.; Zhang, X.H.; et al. A Micromachined Reconfigurable Metamaterial via Reconfiguration of Asymmetric Split-Ring Resonators. *Adv. Funct. Mater.* **2011**, *21*, 3589–3594. [[CrossRef](#)]
35. Zhao, X.; Fan, K.; Zhang, J.; Keiser, G.R.; Duan, G.; Averitt, R.D.; Zhang, X. Voltage-tunable dual-layer terahertz metamaterials. *Microsyst. Nanoeng.* **2016**, *2*, 16025. [[CrossRef](#)]
36. Keiser, G.R.; Seren, H.R.; Strikwerda, A.C.; Zhang, X.; Averitt, R.D. Structural control of metamaterial oscillator strength and electric field enhancement at terahertz frequencies. *Appl. Phys. Lett.* **2014**, *105*, 081112. [[CrossRef](#)]
37. Shadrivov, I.V.; Kozyrev, A.B.; van der Weide, D.W.; Kivshar, Y.S. Tunable transmission and harmonic generation in nonlinear metamaterials. *Appl. Phys. Lett.* **2008**, *93*, 161903. [[CrossRef](#)]
38. Shadrivov, I.V.; Kozyrev, A.B.; van der Weide, D.W.; Kivshar, Y.S. Nonlinear magnetic metamaterials. *Opt. Express* **2008**, *16*, 20266–20271. [[CrossRef](#)] [[PubMed](#)]
39. Powell, D.A.; Shadrivov, I.V.; Kivshar, Y.S. Nonlinear electric metamaterials. *Appl. Phys. Lett.* **2009**, *95*, 084102. [[CrossRef](#)]
40. Lapine, M.; Shadrivov, I.V.; Kivshar, Y.S. Colloquium: Nonlinear metamaterials. *Rev. Mod. Phys.* **2014**, *86*, 1093–1123. [[CrossRef](#)]
41. Rose, A.; Larouche, S.; Huang, D.; Poutrina, E.; Smith, D.R. Nonlinear parameter retrieval from three- and four-wave mixing in metamaterials. *Phys. Rev. E* **2010**, *82*, 036608. [[CrossRef](#)] [[PubMed](#)]
42. Larouche, S.; Smith, D.R. A retrieval method for nonlinear metamaterials. *Opt. Commun.* **2010**, *283*, 1621–1627. [[CrossRef](#)]
43. Huang, D.; Rose, A.; Poutrina, E.; Larouche, S.; Smith, D.R. Wave mixing in nonlinear magnetic metacrystal. *Appl. Phys. Lett.* **2011**, *98*, 204102. [[CrossRef](#)]
44. Larouche, S.; Rose, A.; Poutrina, E.; Huang, D.; Smith, D.R. Experimental determination of the quadratic nonlinear magnetic susceptibility of a varactor-loaded split ring resonator metamaterial. *Appl. Phys. Lett.* **2010**, *97*, 011109. [[CrossRef](#)]
45. Hannam, K.E.; Powell, D.A.; Shadrivov, I.V.; Kivshar, Y.S. Tuning the nonlinear response of coupled split-ring resonators. *Appl. Phys. Lett.* **2012**, *100*, 081111. [[CrossRef](#)]
46. Lapine, M.; Gorkunov, M.; Ringhofer, K.H. Nonlinearity of a metamaterial arising from diode insertions into resonant conductive elements. *Phys. Rev. E* **2003**, *67*, 065601. [[CrossRef](#)] [[PubMed](#)]
47. Lapine, M.; Shadrivov, I.V.; Powell, D.A.; Kivshar, Y.S. Magnetoelastic metamaterials. *Nat. Mater.* **2012**, *11*, 30–33. [[CrossRef](#)] [[PubMed](#)]
48. Rose, A.; Huang, D.; Smith, D.R. Controlling the Second Harmonic in a Phase-Matched Negative-Index Metamaterial. *Phys. Rev. Lett.* **2011**, *107*, 063902. [[CrossRef](#)] [[PubMed](#)]

49. Lange, C.; Maag, T.; Hohenleutner, M.; Baiertl, S.; Schubert, O.; Edwards, E.R.J.; Bougeard, D.; Woltersdorf, G.; Huber, R. Extremely Nonperturbative Nonlinearities in GaAs Driven by Atomically Strong Terahertz Fields in Gold Metamaterials. *Phys. Rev. Lett.* **2014**, *113*, 227401. [[CrossRef](#)] [[PubMed](#)]
50. Keiser, G.R.; Karl, N.; Liu, P.Q.; Tulloss, C.; Chen, H.-T.; Taylor, A.J.; Brener, I.; Reno, J.L.; Mittleman, D.M. Nonlinear terahertz metamaterials with active electrical control. *Appl. Phys. Lett.* **2017**, *111*, 121101. [[CrossRef](#)]
51. Fan, K.; Hwang, H.Y.; Liu, M.; Strikwerda, A.C.; Sternbach, A.; Zhang, J.; Zhao, X.; Zhang, X.; Nelson, K.A.; Averitt, R.D. Nonlinear Terahertz Metamaterials via Field-Enhanced Carrier Dynamics in GaAs. *Phys. Rev. Lett.* **2013**, *110*, 217404. [[CrossRef](#)] [[PubMed](#)]
52. Darrow, J.T.; Zhang, X.; Auston, D.H.; Morse, J.D. Saturation properties of large-aperture photoconducting antennas. *IEEE J. Quantum Electron.* **1992**, *28*, 1607–1616. [[CrossRef](#)]
53. Nuss, M.C.; Auston, D.H.; Capasso, F. Direct Subpicosecond Measurement of Carrier Mobility of Photoexcited Electrons in Gallium Arsenide. *Phys. Rev. Lett.* **1987**, *58*, 2355–2358. [[CrossRef](#)] [[PubMed](#)]
54. Anderson, C.L.; Crowell, C.R. Threshold Energies for Electron-Hole Pair Production by Impact Ionization in Semiconductors. *Phys. Rev. B* **1972**, *5*, 2267–2272. [[CrossRef](#)]
55. Keren-Zur, S.; Avayu, O.; Michaeli, L.; Ellenbogen, T. Nonlinear Beam Shaping with Plasmonic Metasurfaces. *ACS Photonics* **2016**, *3*, 117–123. [[CrossRef](#)]
56. Weis, P.; Garcia-Pomar, J.L.; Beigang, R.; Rahm, M. Hybridization Induced Transparency in Composites of Metamaterials and Atomic Media. *Opt. Express* **2011**, *19*, 23573–23580. [[CrossRef](#)] [[PubMed](#)]
57. Withayachumnankul, W.; Lin, H.; Serita, K.; Shah, C.M.; Sriram, S.; Bhaskaran, M.; Tonouchi, M.; Fumeaux, C.; Abbott, D. Sub-diffraction thin-film sensing with planar terahertz metamaterials. *Opt. Express* **2012**, *20*, 3345–3352. [[CrossRef](#)] [[PubMed](#)]
58. Singh, R.; Al-Naib, I.A.I.; Koch, M.; Zhang, W. Sharp Fano Resonances in THz Metamaterials. *Opt. Express* **2011**, *19*, 6312–6319. [[CrossRef](#)] [[PubMed](#)]
59. Singh, R.; Cao, W.; Al-Naib, I.; Cong, L.; Withayachumnankul, W.; Zhang, W. Ultrasensitive terahertz sensing with high-Q Fano resonances in metasurfaces. *Appl. Phys. Lett.* **2014**, *105*, 171101. [[CrossRef](#)]
60. Yahiaoui, R.; Strikwerda, A.C.; Jepsen, P.U. Terahertz Plasmonic Structure with Enhanced Sensing Capabilities. *IEEE Sens. J.* **2016**, *16*, 2484–2488. [[CrossRef](#)]
61. Suen, J.Y.; Fan, K.; Montoya, J.; Bingham, C.; Stenger, V.; Sriram, S.; Padilla, W.J. Multifunctional metamaterial pyroelectric infrared detectors. *Optica* **2017**, *4*, 276–279. [[CrossRef](#)]
62. Keiser, G.R.; Zhang, J.; Zhao, X.; Zhang, X.; Averitt, R.D. Terahertz saturable absorption in superconducting metamaterials. *J. Opt. Soc. Am. B* **2016**, *33*, 2649–2655. [[CrossRef](#)]
63. Zhao, X.; Zhang, J.; Fan, K.; Duan, G.; Metcalfe, G.D.; Wraback, M.; Zhang, X.; Averitt, R.D. Nonlinear terahertz metamaterial perfect absorbers using GaAs. *Photonics Res.* **2016**, *4*, A16–A21. [[CrossRef](#)]
64. Haus, H. Theory of mode locking with a slow saturable absorber. *IEEE J. Quantum Electron.* **1975**, *11*, 736–746. [[CrossRef](#)]
65. Haus, H.A. Theory of mode locking with a fast saturable absorber. *J. Appl. Phys.* **1975**, *46*, 3049–3058. [[CrossRef](#)]
66. Watts, C.M.; Liu, X.; Padilla, W.J. Metamaterial Electromagnetic Wave Absorbers. *Adv. Mater.* **2012**, *24*, OP98–OP120. [[CrossRef](#)] [[PubMed](#)]
67. Chen, H.-T. Interference theory of metamaterial perfect absorbers. *Opt. Express* **2012**, *20*, 7165–7172. [[CrossRef](#)] [[PubMed](#)]
68. Huang, L.; Chowdhury, D.R.; Ramani, S.; Reiten, M.T.; Luo, S.-N.; Azad, A.K.; Taylor, A.J.; Chen, H.-T. Impact of resonator geometry and its coupling with ground plane on ultrathin metamaterial perfect absorbers. *Appl. Phys. Lett.* **2012**, *101*, 101102. [[CrossRef](#)]
69. Gu, J.; Singh, R.; Tian, Z.; Cao, W.; Xing, Q.; He, M.; Zhang, J.W.; Han, J.; Chen, H.-T.; Zhang, W. Terahertz superconductor metamaterial. *Appl. Phys. Lett.* **2010**, *97*, 071102. [[CrossRef](#)]
70. Ricci, M.; Orloff, N.; Anlage, S.M. Superconducting metamaterials. *Appl. Phys. Lett.* **2005**, *87*, 034102. [[CrossRef](#)]
71. Ricci, M.C.; Hua, X.; Prozorov, R.; Zhuravel, A.P.; Ustinov, A.V.; Anlage, S.M. Tunability of Superconducting Metamaterials. *IEEE Trans. Appl. Supercond.* **2007**, *17*, 918–921. [[CrossRef](#)]
72. Anlage, S.M. The physics and applications of superconducting metamaterials. *J. Opt.* **2011**, *13*, 024001. [[CrossRef](#)]

73. Jung, P.; Ustinov, A.V.; Anlage, S.M. Progress in superconducting metamaterials. *Supercond. Sci. Technol.* **2014**, *27*, 073001. [[CrossRef](#)]
74. Kunchur, M.N.; Christen, D.K.; Klabunde, C.E.; Phillips, J.M. Pair-breaking effect of high current densities on the superconducting transition in $\text{YBaC}_3\text{O}_{7-\delta}$. *Phys. Rev. Lett.* **1994**, *72*, 752–755. [[CrossRef](#)] [[PubMed](#)]
75. Glossner, A.; Zhang, C.; Kikuta, S.; Kawayama, I.; Murakami, H.; Müller, P.; Tonouchi, M. Cooper pair breakup in YBCO under strong terahertz fields. *arXiv* **2012**, arXiv:1205.1684.
76. Geier, A.; Schön, G. Response of a superconductor to a supercritical current pulse. *J. Low Temp. Phys.* **1982**, *46*, 151–160. [[CrossRef](#)]
77. Hu, T.; Strikwerda, A.C.; Fan, K.; Bingham, C.M.; Padilla, W.J.; Xin, Z.; Averitt, R.D. Terahertz metamaterials on free-standing highly-flexible polyimide substrates. *J. Phys. D Appl. Phys.* **2008**, *41*, 232004.
78. Vitiello, M.S.; Scalari, G.; Williams, B.; De Natale, P. Quantum cascade lasers: 20 years of challenges. *Opt. Express* **2015**, *23*, 5167–5182. [[CrossRef](#)] [[PubMed](#)]
79. Vitiello, M.S.; Scamarcio, G.; Spagnolo, V.; Dhillon, S.S.; Sirtori, C. Terahertz quantum cascade lasers with large wall-plug efficiency. *Appl. Phys. Lett.* **2007**, *90*, 191115. [[CrossRef](#)]
80. Hwang, H.Y.; Fleischer, S.; Brandt, N.C.; Perkins, B.G.; Liu, M.; Fan, K.; Sternbach, A.; Zhang, X.; Averitt, R.D.; Nelson, K.A. A review of non-linear terahertz spectroscopy with ultrashort tabletop-laser pulses. *J. Mod. Opt.* **2014**, *62*, 1447–1479. [[CrossRef](#)]
81. Goodenough, J.B. The two components of the crystallographic transition in VO_2 . *J. Solid State Chem.* **1971**, *3*, 490–500. [[CrossRef](#)]
82. Cavalleri, A.; Dekorsy, T.; Chong, H.H.W.; Kieffer, J.C.; Schoenlein, R.W. Evidence for a structurally-driven insulator-to-metal transition in VO_2 : A view from the ultrafast timescale. *Phys. Rev. B* **2004**, *70*, 161102. [[CrossRef](#)]
83. Laverock, J.; Kittiwatanakul, S.; Zakharov, A.A.; Niu, Y.R.; Chen, B.; Wolf, S.A.; Lu, J.W.; Smith, K.E. Direct Observation of Decoupled Structural and Electronic Transitions and an Ambient Pressure Monocliniclike Metallic Phase of VO_2 . *Phys. Rev. Lett.* **2014**, *113*, 216402. [[CrossRef](#)] [[PubMed](#)]
84. Gray, A.X.; Hoffmann, M.C.; Jeong, J.; Aetukuri, N.P.; Zhu, D.; Hwang, H.Y.; Brandt, N.C.; Wen, H.; Sternbach, A.J.; Bonetti, S.; et al. Ultrafast terahertz field control of electronic and structural interactions in vanadium dioxide. *Phys. Rev. B* **2018**, *98*, 045104. [[CrossRef](#)]
85. Pein, B.C.; Chang, W.; Hwang, H.Y.; Scherer, J.; Coropceanu, I.; Zhao, X.; Zhang, X.; Bulović, V.; Bawendi, M.; Nelson, K.A. Terahertz-Driven Luminescence and Colossal Stark Effect in CdSe-CdS Colloidal Quantum Dots. *Nano Lett.* **2017**, *17*, 5375–5380. [[CrossRef](#)] [[PubMed](#)]
86. Empedocles, S.A.; Bawendi, M.G. Quantum-Confined Stark Effect in Single CdSe Nanocrystallite Quantum Dots. *Science* **1997**, *278*, 2114. [[CrossRef](#)] [[PubMed](#)]
87. Hoffmann, M.C.; Monozon, B.S.; Livshits, D.; Rafailov, E.U.; Turchinovich, D. Terahertz electro-absorption effect enabling femtosecond all-optical switching in semiconductor quantum dots. *Appl. Phys. Lett.* **2010**, *97*, 231108. [[CrossRef](#)]
88. Kyoung, J.; Seo, M.; Park, H.; Koo, S.; Kim, H.S.; Park, Y.; Kim, B.J.; Ahn, K.; Park, N.; Kim, H.T.; et al. Giant nonlinear response of terahertz nanoresonators on VO_2 thin film. *Opt. Express* **2010**, *18*, 16452–16459. [[CrossRef](#)] [[PubMed](#)]
89. Kim, J.Y.; Kang, B.J.; Park, J.; Bahk, Y.M.; Kim, W.T.; Rhie, J.; Jeon, H.; Rotermund, F.; Kim, D.S. Terahertz Quantum Plasmonics of Nanoslot Antennas in Nonlinear Regime. *Nano Lett.* **2015**, *15*, 6683–6688. [[CrossRef](#)] [[PubMed](#)]
90. Ryu, Y.S.; Lee, D.K.; Kang, J.H.; Lee, S.H.; Yu, E.S.; Seo, M. Ultrasensitive terahertz sensing of gold nanoparticles inside nano slot antennas. *Opt. Express* **2017**, *25*, 30591–30597. [[CrossRef](#)] [[PubMed](#)]
91. Seo, M.A.; Park, H.R.; Koo, S.M.; Park, D.J.; Kang, J.H.; Suwal, O.K.; Choi, S.S.; Planken, P.C.M.; Park, G.S.; Park, N.K.; et al. Terahertz field enhancement by a metallic nano slit operating beyond the skin-depth limit. *Nat. Photonics* **2009**, *3*, 152–156. [[CrossRef](#)]
92. Klarskov, P.; Tarekgegne, A.T.; Iwaszczuk, K.; Zhang, X.C.; Jepsen, P.U. Amplification of resonant field enhancement by plasmonic lattice coupling in metallic slit arrays. *Sci. Rep.* **2016**, *6*, 37738. [[CrossRef](#)] [[PubMed](#)]
93. Park, H.R.; Ahn, K.J.; Han, S.; Bahk, Y.M.; Park, N.; Kim, D.S. Colossal absorption of molecules inside single terahertz nanoantennas. *Nano Lett.* **2013**, *13*, 1782–1786. [[CrossRef](#)] [[PubMed](#)]

94. Lee, D.-K.; Kim, G.; Kim, C.; Jhon, Y.M.; Kim, J.H.; Lee, T.; Son, J.-H.; Seo, M. Ultrasensitive Detection of Residual Pesticides Using THz Near-Field Enhancement. *IEEE Trans. Terahertz Sci. Technol.* **2016**, *6*, 389–395. [[CrossRef](#)]
95. Lee, D.K.; Kang, J.H.; Lee, J.S.; Kim, H.S.; Kim, C.; Kim, J.H.; Lee, T.; Son, J.H.; Park, Q.H.; Seo, M. Highly sensitive and selective sugar detection by terahertz nano-antennas. *Sci. Rep.* **2015**, *5*, 15459. [[CrossRef](#)] [[PubMed](#)]
96. Choi, G.; Bahk, Y.M.; Kang, T.; Lee, Y.; Son, B.H.; Ahn, Y.H.; Seo, M.; Kim, D.S. Terahertz Nanoprobing of Semiconductor Surface Dynamics. *Nano Lett.* **2017**, *17*, 6397–6401. [[CrossRef](#)] [[PubMed](#)]
97. Bitzer, A.; Wallauer, J.; Helm, H.; Merbold, H.; Feurer, T.; Walther, M. Lattice modes mediate radiative coupling in metamaterial arrays. *Opt. Express* **2009**, *17*, 22108–22113. [[CrossRef](#)] [[PubMed](#)]
98. Tan, T.C.; Srivastava, Y.K.; Manjappa, M.; Plum, E.; Singh, R. Lattice induced strong coupling and line narrowing of split resonances in metamaterials. *Appl. Phys. Lett.* **2018**, *112*, 201111. [[CrossRef](#)]
99. Adam, A.J.L. Review of Near-Field Terahertz Measurement Methods and Their Applications. *J. Infrared Millim. Terahertz Waves* **2011**, *32*, 976–1019. [[CrossRef](#)]
100. Mittleman, D.M. Twenty years of terahertz imaging. *Opt. Express* **2018**, *26*, 9417. [[CrossRef](#)] [[PubMed](#)]
101. Hunsche, S.; Koch, M.; Brener, I.; Nuss, M.C. THz near-field imaging. *Opt. Commun.* **1998**, *150*, 22–26. [[CrossRef](#)]
102. Liu, S.; Mitrofanov, O.; Nahata, A. Near-field terahertz imaging using sub-wavelength apertures without cutoff. *Opt. Express* **2016**, *24*, 2728–2736. [[CrossRef](#)] [[PubMed](#)]
103. Nguyen, T.D.; Vardeny, Z.V.; Nahata, A. Concentration of terahertz radiation through a conically tapered aperture. *Opt. Express* **2010**, *18*, 25441–25448. [[CrossRef](#)] [[PubMed](#)]
104. Kim, S.H.; Lee, E.S.; Ji, Y.B.; Jeon, T.I. Improvement of THz coupling using a tapered parallel-plate waveguide. *Opt. Express* **2010**, *18*, 1289–1295. [[CrossRef](#)] [[PubMed](#)]
105. Theuer, M.; Harsha, S.S.; Grischkowsky, D. Flare coupled metal parallel-plate waveguides for high resolution terahertz time-domain spectroscopy. *J. Appl. Phys.* **2010**, *108*, 113105. [[CrossRef](#)]
106. Macfaden, A.J.; Reno, J.L.; Brener, I.; Mitrofanov, O. 3 μm aperture probes for near-field terahertz transmission microscopy. *Appl. Phys. Lett.* **2014**, *104*, 011110. [[CrossRef](#)]
107. Zhan, H.; Mendis, R.; Mittleman, D.M. Superfocusing terahertz waves below $\lambda/250$ using plasmonic parallel-plate waveguides. *Opt. Express* **2010**, *18*, 9643–9650. [[CrossRef](#)] [[PubMed](#)]
108. Iwaszczuk, K.; Andryieuski, A.; Lavrinenko, A.; Zhang, X.C.; Jepsen, P.U. Terahertz field enhancement to the MV/cm regime in a tapered parallel plate waveguide. *Opt. Express* **2012**, *20*, 8344–8355. [[CrossRef](#)] [[PubMed](#)]
109. Reichel, K.S.; Iwaszczuk, K.; Jepsen, P.U.; Mendis, R.; Mittleman, D.M. In situ spectroscopic characterization of a terahertz resonant cavity. *Optica* **2014**, *1*, 272–275. [[CrossRef](#)]
110. Klein, N.; Lahl, P.; Poppe, U.; Kadlec, F.; Kužel, P. A metal-dielectric antenna for terahertz near-field imaging. *J. Appl. Phys.* **2005**, *98*, 014910. [[CrossRef](#)]
111. Tuniz, A.; Kaltenecker, K.J.; Fischer, B.M.; Walther, M.; Fleming, S.C.; Argyros, A.; Kuhlmeier, B.T. Metamaterial fibres for subdiffraction imaging and focusing at terahertz frequencies over optically long distances. *Nat. Commun.* **2013**, *4*, 2706. [[CrossRef](#)] [[PubMed](#)]
112. Wächter, M.; Nagel, M.; Kurz, H. Tapered photoconductive terahertz field probe tip with subwavelength spatial resolution. *Appl. Phys. Lett.* **2009**, *95*, 041112. [[CrossRef](#)]
113. Rusina, A.; Durach, M.; Nelson, K.A.; Stockman, M.I. Nanoconcentration of terahertz radiation in plasmonic waveguides. *Opt. Express* **2008**, *16*, 18576–18589. [[CrossRef](#)] [[PubMed](#)]
114. Atkin, J.M.; Berweger, S.; Jones, A.C.; Raschke, M.B. Nano-optical imaging and spectroscopy of order, phases, and domains in complex solids. *Adv. Phys.* **2012**, *61*, 745–842. [[CrossRef](#)]
115. Berweger, S.; Atkin, J.M.; Olmon, R.L.; Raschke, M.B. Light on the Tip of a Needle: Plasmonic Nanofocusing for Spectroscopy on the Nanoscale. *J. Phys. Chem. Lett.* **2012**, *3*, 945–952. [[CrossRef](#)] [[PubMed](#)]
116. Qazilbash, M.M.; Brehm, M.; Chae, B.G.; Ho, P.C.; Andreev, G.O.; Kim, B.J.; Yun, S.J.; Balatsky, A.V.; Maple, M.B.; Keilmann, F.; et al. Mott transition in VO₂ revealed by infrared spectroscopy and nano-imaging. *Science* **2007**, *318*, 1750–1753. [[CrossRef](#)] [[PubMed](#)]
117. Fei, Z.; Andreev, G.O.; Bao, W.; Zhang, L.M.; Alexander, S.M.; Wang, C.; Stewart, M.K.; Zhao, Z.; Dominguez, G.; Thiemens, M.; et al. Infrared nanoscopy of dirac plasmons at the graphene-SiO₂ interface. *Nano Lett.* **2011**, *11*, 4701–4705. [[CrossRef](#)] [[PubMed](#)]

118. Zenhausern, F.; Martin, Y.; Wickramasinghe, H.K. Scanning Interferometric Apertureless Microscopy: Optical Imaging at 10 Angstrom Resolution. *Science* **1995**, *269*, 1083–1085. [[CrossRef](#)] [[PubMed](#)]
119. Fei, Z.; Foley IV, J.J.; Gannett, W.; Liu, M.K.; Dai, S.; Ni, G.X.; Zettl, A.; Fogler, M.M.; Wiederrecht, G.P.; Gray, S.K.; et al. Ultraconfined Plasmonic Hotspots inside Graphene Nanobubbles. *Nano Lett.* **2016**, *16*, 7842–7848. [[CrossRef](#)] [[PubMed](#)]
120. Huber, M.A.; Mooshammer, F.; Plankl, M.; Viti, L.; Sandner, F.; Kastner, L.Z.; Frank, T.; Fabian, J.; Vitiello, M.S.; Cocker, T.L.; et al. Femtosecond photo-switching of interface polaritons in black phosphorus heterostructures. *Nat. Nanotechnol.* **2017**, *12*, 207–211. [[CrossRef](#)] [[PubMed](#)]
121. Knoll, B.; Keilmann, F.; Kramer, A.; Guckenberger, R. Contrast of microwave near-field microscopy. *Appl. Phys. Lett.* **1997**, *70*, 2667–2669. [[CrossRef](#)]
122. Knoll, B.; Keilmann, F. Near-field probing of vibrational absorption for chemical microscopy. *Nature* **1999**, *399*, 20154. [[CrossRef](#)]
123. Chen, H.-T.; Kersting, R.; Cho, G.C. Terahertz imaging with nanometer resolution. *Appl. Phys. Lett.* **2003**, *83*, 3009–3011. [[CrossRef](#)]
124. Keilmann, F.; Hillenbrand, R. Near-field microscopy by elastic light scattering from a tip. *Philos. Trans. A Math. Phys. Eng. Sci.* **2004**, *362*, 787–805. [[CrossRef](#)] [[PubMed](#)]
125. Knoll, B.; Keilmann, F. Enhanced dielectric contrast in scattering-type scanning near-field optical microscopy. *Opt. Commun.* **2000**, *182*, 321–328. [[CrossRef](#)]
126. Cvitkovic, A.; Ocelic, N.; Hillenbrand, R. Analytical model for quantitative prediction of material contrasts in scattering-type near-field optical microscopy. *Opt. Express* **2007**, *15*, 8550–8565. [[CrossRef](#)] [[PubMed](#)]
127. Govyadinov, A.A.; Amenabar, I.; Huth, F.; Carney, P.S.; Hillenbrand, R. Quantitative Measurement of Local Infrared Absorption and Dielectric Function with Tip-Enhanced Near-Field Microscopy. *J. Phys. Chem. Lett.* **2013**, *4*, 1526–1531. [[CrossRef](#)] [[PubMed](#)]
128. Huber, A.J.; Keilmann, F.; Wittborn, J.; Aizpurua, J.; Hillenbrand, R. Terahertz Near-Field Nanoscopy of Mobile Carriers in Single Semiconductor Nanodevices. *Nano Lett.* **2008**, *8*, 3766–3770. [[CrossRef](#)] [[PubMed](#)]
129. Giordano, M.C.; Mastel, S.; Liewald, C.; Columbo, L.L.; Brambilla, M.; Viti, L.; Politano, A.; Zhang, K.; Li, L.; Davies, A.G.; et al. Phase-resolved terahertz self-detection near-field microscopy. *Opt. Express* **2018**, *26*, 18423–18435. [[CrossRef](#)] [[PubMed](#)]
130. Liewald, C.; Mastel, S.; Hesler, J.; Huber, A.J.; Hillenbrand, R.; Keilmann, F. All-electronic terahertz nanoscopy. *Optica* **2018**, *5*, 159. [[CrossRef](#)]
131. Degl'Innocenti, R.; Wallis, R.; Wei, B.; Xiao, L.; Kindness, S.J.; Mitrofanov, O.; Braeuninger-Weimer, P.; Hofmann, S.; Beere, H.E.; Ritchie, D.A. Terahertz Nanoscopy of Plasmonic Resonances with a Quantum Cascade Laser. *ACS Photonics* **2017**, *4*, 2150–2157. [[CrossRef](#)]
132. Kuschewski, F.; von Ribbeck, H.G.; Döring, J.; Winnerl, S.; Eng, L.M.; Kehr, S.C. Narrow-band near-field nanoscopy in the spectral range from 1.3 to 8.5 THz. *Appl. Phys. Lett.* **2016**, *108*, 113102. [[CrossRef](#)]
133. Kehr, S.C.; Döring, J.; Gensch, M.; Helm, M.; Eng, L.M. FEL-Based Near-Field Infrared to THz Nanoscopy. *Synchrotron Radiat. News* **2017**, *30*, 31–35. [[CrossRef](#)]
134. Moon, K.; Park, H.; Kim, J.; Do, Y.; Lee, S.; Lee, G.; Kang, H.; Han, H. Subsurface nanoimaging by broadband terahertz pulse near-field microscopy. *Nano Lett.* **2015**, *15*, 549–552. [[CrossRef](#)] [[PubMed](#)]
135. Wang, K.; Mittleman, D.M.; van der Valk, N.C.J.; Planken, P.C.M. Antenna effects in terahertz apertureless near-field optical microscopy. *Appl. Phys. Lett.* **2004**, *85*, 2715–2717. [[CrossRef](#)]
136. Wang, K.; Barkan, A.; Mittleman, D.M. Propagation effects in apertureless near-field optical antennas. *Appl. Phys. Lett.* **2004**, *84*, 305–307. [[CrossRef](#)]
137. Zhan, H.; Astley, V.; Hvasta, M.; Deibel, J.A.; Mittleman, D.M.; Lim, Y.-S. The metal-insulator transition in VO₂ studied using terahertz apertureless near-field microscopy. *Appl. Phys. Lett.* **2007**, *91*, 162110. [[CrossRef](#)]
138. Moon, K.; Do, Y.; Lim, M.; Lee, G.; Kang, H.; Park, K.-S.; Han, H. Quantitative coherent scattering spectra in apertureless terahertz pulse near-field microscopes. *Appl. Phys. Lett.* **2012**, *101*, 011109. [[CrossRef](#)]
139. Zhang, J.W.; Chen, X.Z.; Mills, S.; Ciavatti, T.; Yao, Z.H.; Mescall, R.; Hu, H.; Semenenko, V.; Fei, Z.; Li, H.; et al. Terahertz Nanoimaging of Graphene. *ACS Photonics* **2018**, *5*, 2645–2651. [[CrossRef](#)]
140. Krutokhvostov, R.; Govyadinov, A.A.; Stiegler, J.M.; Huth, F.; Chuvilin, A.; Carney, P.S.; Hillenbrand, R. Enhanced resolution in subsurface near-field optical microscopy. *Opt. Express* **2012**, *20*, 593–600. [[CrossRef](#)] [[PubMed](#)]

141. Eisele, M.; Cocker, T.L.; Huber, M.A.; Plankl, M.; Viti, L.; Ercolani, D.; Sorba, L.; Vitiello, M.S.; Huber, R. Ultrafast multi-terahertz nano-spectroscopy with sub-cycle temporal resolution. *Nat. Photonics* **2014**, *8*, 841–845. [[CrossRef](#)]
142. Alonso-Gonzalez, P.; Nikitin, A.Y.; Gao, Y.; Woessner, A.; Lundeberg, M.B.; Principi, A.; Forcellini, N.; Yan, W.; Velez, S.; Huber, A.J.; et al. Acoustic terahertz graphene plasmons revealed by photocurrent nanoscopy. *Nat. Nanotechnol.* **2017**, *12*, 31–35. [[CrossRef](#)] [[PubMed](#)]
143. Lundeberg, M.B.; Gao, Y.; Woessner, A.; Tan, C.; Alonso-González, P.; Watanabe, K.; Taniguchi, T.; Hone, J.; Hillenbrand, R.; Koppens, F.H.L. Thermoelectric detection and imaging of propagating graphene plasmons. *Nat. Mater.* **2016**, *16*, 204–207. [[CrossRef](#)] [[PubMed](#)]
144. Woessner, A.; Alonso-González, P.; Lundeberg, M.B.; Gao, Y.; Barrios-Vargas, J.E.; Navickaite, G.; Ma, Q.; Janner, D.; Watanabe, K.; Cummings, A.W.; et al. Near-field photocurrent nanoscopy on bare and encapsulated graphene. *Nat. Commun.* **2016**, *7*, 10783. [[CrossRef](#)] [[PubMed](#)]
145. Murakami, H.; Uchida, N.; Inoue, R.; Kim, S.; Kiwa, T.; Tonouchi, M. Laser Terahertz Emission Microscope. *Proc. IEEE* **2007**, *95*, 1646–1657. [[CrossRef](#)]
146. Kiwa, T.; Tonouchi, M.; Yamashita, M.; Kawase, K. Laser terahertz-emission microscope for inspecting electrical faults in integrated circuits. *Opt. Lett.* **2003**, *28*, 2058–2060. [[CrossRef](#)] [[PubMed](#)]
147. Tonouchi, M.; Yamashita, M.; Hangyo, M. Terahertz radiation imaging of supercurrent distribution in vortex-penetrated $\text{YBa}_2\text{Cu}_3\text{O}_{7-\delta}$ thin film strips. *J. Appl. Phys.* **2000**, *87*, 7366–7375. [[CrossRef](#)]
148. Suzuki, M.; Tonouchi, M.; Fujii, K.-I.; Ohtake, H.; Hirosumi, T. Excitation wavelength dependence of terahertz emission from semiconductor surface. *Appl. Phys. Lett.* **2006**, *89*, 091111. [[CrossRef](#)]
149. Rana, D.S.; Takahashi, K.; Mavani, K.R.; Kawayama, I.; Murakami, H.; Tonouchi, M. Visualization of photoassisted polarization switching and its consequences in BiFeO_3 thin films probed by terahertz radiation. *Appl. Phys. Lett.* **2007**, *91*, 031909. [[CrossRef](#)]
150. Nakanishi, H.; Fujiwara, S.; Takayama, K.; Kawayama, I.; Murakami, H.; Tonouchi, M. Imaging of a Polycrystalline Silicon Solar Cell Using a Laser Terahertz Emission Microscope. *Appl. Phys. Express* **2012**, *5*, 112301. [[CrossRef](#)]
151. Kushnir, K.; Wang, M.; Fitzgerald, P.D.; Koski, K.J.; Titova, L.V. Ultrafast Zero-Bias Photocurrent in GeS Nanosheets: Promise for Photovoltaics. *ACS Energy Lett.* **2017**, *2*, 1429–1434. [[CrossRef](#)]
152. Sanjuan, F.; Gaborit, G.; Coutaz, J.L. Sub-wavelength terahertz imaging through optical rectification. *Sci. Rep.* **2018**, *8*, 13492. [[CrossRef](#)] [[PubMed](#)]
153. Sano, Y.; Kawayama, I.; Tabata, M.; Salek, K.A.; Murakami, H.; Wang, M.; Vajtai, R.; Ajayan, P.M.; Kono, J.; Tonouchi, M. Imaging molecular adsorption and desorption dynamics on graphene using terahertz emission spectroscopy. *Sci. Rep.* **2014**, *4*, 6046. [[CrossRef](#)] [[PubMed](#)]
154. Sakai, Y.; Kawayama, I.; Nakanishi, H.; Tonouchi, M. Visualization of GaN surface potential using terahertz emission enhanced by local defects. *Sci. Rep.* **2015**, *5*, 13860. [[CrossRef](#)] [[PubMed](#)]
155. Mochizuki, T.; Ito, A.; Mitchell, J.; Nakanishi, H.; Tanahashi, K.; Kawayama, I.; Tonouchi, M.; Shirasawa, K.; Takato, H. Probing the surface potential of oxidized silicon by assessing terahertz emission. *Appl. Phys. Lett.* **2017**, *110*, 163502. [[CrossRef](#)]
156. Klarskov, P.; Kim, H.; Colvin, V.L.; Mittleman, D.M. Nanoscale Laser Terahertz Emission Microscopy. *ACS Photonics* **2017**, *4*, 2676–2680. [[CrossRef](#)]
157. Liu, K.; Xu, J.; Yuan, T.; Zhang, X.C. Terahertz radiation from InAs induced by carrier diffusion and drift. *Phys. Rev. B* **2006**, *73*, 155330. [[CrossRef](#)]
158. Huber, M.A.; Plankl, M.; Eisele, M.; Marvel, R.E.; Sandner, F.; Korn, T.; Schuller, C.; Haglund, R.F., Jr.; Huber, R.; Cocker, T.L. Ultrafast Mid-Infrared Nanoscopy of Strained Vanadium Dioxide Nanobeams. *Nano Lett.* **2016**, *16*, 1421–1427. [[CrossRef](#)] [[PubMed](#)]
159. Huth, F.; Chuvilin, A.; Schnell, M.; Amenabar, I.; Krutokhvostov, R.; Lopatin, S.; Hillenbrand, R. Resonant antenna probes for tip-enhanced infrared near-field microscopy. *Nano Lett.* **2013**, *13*, 1065–1072. [[CrossRef](#)] [[PubMed](#)]
160. Mastel, S.; Lundeberg, M.B.; Alonso-Gonzalez, P.; Gao, Y.; Watanabe, K.; Taniguchi, T.; Hone, J.; Koppens, F.H.L.; Nikitin, A.Y.; Hillenbrand, R. Terahertz Nanofocusing with Cantilevered Terahertz-Resonant Antenna Tips. *Nano Lett.* **2017**, *17*, 6526–6533. [[CrossRef](#)] [[PubMed](#)]
161. Siday, T.; Natrella, M.; Wu, J.; Liu, H.; Mitrofanov, O. Resonant terahertz probes for near-field scattering microscopy. *Opt. Express* **2017**, *25*, 27874–27885. [[CrossRef](#)] [[PubMed](#)]

162. Kalkbrenner, T.; Ramstein, M.; Mlynek, J.; Sandoghdar, V. A single gold particle as a probe for apertureless scanning near-field optical microscopy. *J. Microsc.* **2001**, *202*, 72–76. [[CrossRef](#)] [[PubMed](#)]
163. Mitrofanov, O.; Lee, M.; Hsu, J.W.P.; Brener, I.; Harel, R.; Federici, J.F.; Wynn, J.D.; Pfeiffer, L.N.; West, K.W. Collection-mode near-field imaging with 0.5-THz pulses. *IEEE J. Sel. Top. Quantum Electron.* **2001**, *7*, 600–607. [[CrossRef](#)]
164. Ishihara, K.; Ohashi, K.; Ikari, T.; Minamide, H.; Yokoyama, H.; Shikata, J.-I.; Ito, H. Terahertz-wave near-field imaging with subwavelength resolution using surface-wave-assisted bow-tie aperture. *Appl. Phys. Lett.* **2006**, *89*, 201120. [[CrossRef](#)]
165. Bitzer, A.; Ortner, A.; Walther, M. Terahertz near-field microscopy with subwavelength spatial resolution based on photoconductive antennas. *Appl. Opt.* **2010**, *49*, E1–E6. [[CrossRef](#)] [[PubMed](#)]
166. Blanchard, F.; Doi, A.; Tanaka, T.; Hirori, H.; Tanaka, H.; Kadoya, Y.; Tanaka, K. Real-time terahertz near-field microscope. *Opt. Express* **2011**, *19*, 8277–8284. [[CrossRef](#)] [[PubMed](#)]
167. van der Valk, N.C.J.; Planken, P.C.M. Electro-optic detection of subwavelength terahertz spot sizes in the near field of a metal tip. *Appl. Phys. Lett.* **2002**, *81*, 1558–1560. [[CrossRef](#)]
168. Yuan, T.; Park, H.; Xu, J.; Han, H.; Zhang, X.C. THz Wave Near-Field Emission Microscope. In *Ultrafast Phenomena XIV*; Kobayashi, T., Okada, T., Kobayashi, T., Nelson, K.A., De Silvestri, S., Eds.; Springer: Berlin/Heidelberg, Germany, 2005; Volume 79, pp. 759–761.
169. Knoll, B.; Keilmann, F. Mid-infrared scanning near-field optical microscope resolves 30 nm. *J. Microsc.* **1999**, *194*, 512–515. [[CrossRef](#)] [[PubMed](#)]
170. Mastel, S.; Govyadinov, A.A.; Maissen, C.; Chuvilin, A.; Berger, A.; Hillenbrand, R. Understanding the Image Contrast of Material Boundaries in IR Nanoscopy Reaching 5 nm Spatial Resolution. *ACS Photonics* **2018**, *5*, 3372–3378. [[CrossRef](#)]
171. Hell, S.W.; Wichmann, J. Breaking the diffraction resolution limit by stimulated emission: Stimulated-emission-depletion fluorescence microscopy. *Opt. Lett.* **1994**, *19*, 780–782. [[CrossRef](#)] [[PubMed](#)]



© 2019 by the authors. Licensee MDPI, Basel, Switzerland. This article is an open access article distributed under the terms and conditions of the Creative Commons Attribution (CC BY) license (<http://creativecommons.org/licenses/by/4.0/>).